


**Effect of frequency-dependent shear and volume viscosities on molecular friction in liquids**

Henrik Kiefer , Domenico Vitali , Benjamin A. Dalton , Laura Scalfi , and Roland R. Netz <sup>\*</sup>  
*Fachbereich Physik, Freie Universität Berlin, Arnimallee 14, 14195 Berlin, Germany*

 (Received 23 August 2024; accepted 5 December 2024; published 23 January 2025)

The relation between the frequency-dependent friction of a molecule in a liquid and the hydrodynamic properties of the liquid is fundamental for molecular dynamics. We investigate this connection for a water molecule moving in liquid water using all-atomistic molecular dynamics (MD) simulations and linear hydrodynamic theory. We analytically calculate the frequency-dependent friction of a sphere with finite surface slip moving in a viscoelastic compressible fluid by solving the linear transient Stokes equation, including frequency-dependent shear and volume viscosities, both determined from MD simulations of bulk liquid water. From MD simulation trajectories, we also determine the frequency-dependent friction of a single water molecule moving in liquid water, as defined by the generalized Langevin equation. The frequency dependence of the shear viscosity of liquid water requires careful consideration of hydrodynamic finite-size effects to observe the asymptotic hydrodynamic power-law tail. By fitting the effective sphere radius and the slip length, the frequency-dependent friction and velocity autocorrelation function from the transient Stokes equation and simulations quantitatively agree. This shows that the transient Stokes equation accurately describes the important features of the frequency-dependent friction of a single water molecule in liquid water and thus applies down to molecular length and time scales, provided accurate frequency-dependent viscosities are used. In contrast, for a methane molecule moving in water, the frequency-dependent friction cannot be predicted based on a homogeneous model, which, supported by the extraction of the frequency-dependent surface slip, suggests that a methane molecule is surrounded by a finite-thickness hydration layer with viscoelastic properties that differ significantly from those of bulk water.

DOI: [10.1103/PhysRevE.111.015104](https://doi.org/10.1103/PhysRevE.111.015104)

**I. INTRODUCTION**

The friction force acting on a solute molecule in a liquid environment exhibits a delayed non-Markovian response due to the finite relaxation time of the solvating liquid degrees of freedom [1–5]. Such memory effects occur on time scales that range between subpicoseconds up to microseconds and even seconds, depending on the type and complexity of the system [6–10]. Including time- or frequency-dependent friction in an appropriate theoretical framework allows for the accurate modeling of macromolecular dynamics in liquid environments [11–15] and for the proper viscoelastic description of soft matter [16–19]. A fundamental question concerns the connection between the macroscopic hydrodynamic equations and the molecular friction acting on a particle or a molecule in a fluid. Numerous studies investigated this connection by comparing the frequency-dependent friction acting on a particle, as described by the generalized Langevin equation, with the friction obtained by solving the hydrodynamic equations for the fluid flow around a spherical particle [20–29]. Pioneering work in this direction was done by Zwanzig *et al.*

[30] and later by Metiu *et al.* [31], who obtained the time- or frequency-dependent friction by solving the linearized Stokes equation for a spherical particle in the presence of a frequency-dependent shear viscosity, described by a Maxwell model with a single relaxation time.

Since a considerable discrepancy between the friction obtained from the solution of the Stokes equation and the friction derived from the velocity autocorrelations obtained in molecular dynamics simulations was found, especially at high frequencies, it was concluded that hydrodynamic theory does not work on molecular time and length scales [30,31]. Such a breakdown of hydrodynamics would most plausibly be explained by spatial nonlocality in the fluidic viscous response, which in principle could be treated in reciprocal space but would render the Stokes solution for the frequency-dependent friction around a sphere invalid. However, a critical limitation in the comparison in Refs. [30,31] is that a Maxwell model with a single relaxation time was used for the shear viscosity in the solution of the Stokes equation. In fact, viscosity spectra measured in experiments [32,33] and extracted from molecular dynamics (MD) simulations of water [34–36] indicate pronounced deviations from a simple Maxwell model, especially at high frequencies in the THz regime. This is the frequency range where deviations between the friction from hydrodynamic predictions and molecular simulation were found, so it is unclear whether spatially homogeneous hydrodynamic theory breaks down or whether an inappropriate model for the shear viscosity was used.

<sup>\*</sup>Contact author: [metz@physik.fu-berlin.de](mailto:metz@physik.fu-berlin.de)

*Published by the American Physical Society under the terms of the Creative Commons Attribution 4.0 International license. Further distribution of this work must maintain attribution to the author(s) and the published article's title, journal citation, and DOI.*

In the present work, we reconsider the connection between macroscopic hydrodynamics and molecular friction; for this, we consider a single water molecule in a liquid water environment. We first analytically calculate the frequency-dependent friction acting on a sphere using the linearized Stokes equation in the presence of frequency-dependent shear and volume viscosities, finite compressibility, and a finite surface slip [37]. In contrast with previous work [26,27,30,31] we do not use a phenomenological Maxwell model for the viscosities but rather employ frequency-dependent shear and volume viscosities extracted from MD simulations. We investigate in detail the influence of compressibility and the frequency dependence of the volume viscosity on the friction function at high frequencies. Finally, we compare the friction calculated from the transient Stokes equation with the friction extracted from MD simulations using the framework of the generalized Langevin equation.

Using the surface-slip parameter and the sphere radius that appear in the hydrodynamic prediction of the friction as free fit parameters, we find that the frequency-dependent friction of a water molecule extracted directly from MD simulations is in good agreement with the hydrodynamic predictions for frequencies up to 10 THz. This establishes the long-sought link between macroscopic hydrodynamics and the friction acting on a molecule in a fluid and shows that the continuum hydrodynamic equations work for water down to the scale of a single water molecule.

It turns out that the macroscopic shear viscosity of water shows pronounced multimodal behavior as a function of frequency and thus cannot be described by a Maxwell model with a single relaxation time, which explains why previous attempts to derive the frequency-dependent molecular friction from hydrodynamic theory failed. The fitted hydrodynamic radius and slip length obtained from our comparison agree with recent results extracted from the translational and rotational diffusivities of a water molecule in liquid water [38], which demonstrates that our approach is physically sound.

The friction calculated from the Stokes equation exhibits a power-law tail for long times, attributed to the so-called Basset-Boussinesq force [39–41]. However, on the time scales reachable with MD simulations of water, the long time tail, which corresponds to a negative friction force, is completely dominated by the frequency-dependent shear viscosity, which produces positive friction up to times of a few picoseconds and is for longer times masked by finite-size effects [42–44], in perfect agreement between our hydrodynamic predictions and the MD simulation results. Our findings are supported by a comparison of the velocity autocorrelation function computed from the MD simulation and from the hydrodynamic friction including frequency-dependent viscosities and finite compressibility.

We thus find that the macroscopic hydrodynamic equations work surprisingly well down to molecular time and spatial scales for homogeneous water, i.e., if one considers the motion of a single water molecule embedded in liquid water, if and only if the frequency-dependent shear viscosity of water is used. This shows that a wave-vector-dependent viscosity, which would appear in a formally exact formulation of the linear-response stress-strain relation, is not necessary.

In contrast, the friction of a single methane molecule in liquid water is not well described by hydrodynamic theory using liquid water shear and volume viscosities. A reasonable extension of the theory is the introduction of a frequency-dependent slip coefficient. We therefore calculate the frequency-dependent slip which leads to a perfect accordance between the friction of the MD simulation and hydrodynamic theory. The surface-slip spectrum of a methane molecule in water is negative for a finite frequency range, indicating that the local viscosity around methane is enhanced compared with the macroscopic water shear viscosity. It is known that methane in water is surrounded by a clathrate-like highly ordered structure. We thus conclude that, for inhomogeneous liquids, i.e., for the motion of a molecule that differs from the surrounding liquid, a homogeneous hydrodynamic model has to be generalized to account for the possibly modified viscosity of the solvation layer around a moving guest molecule, as recently found for nanoscopic tracer beads moving in hydrogels [45].

## II. THEORY

### A. Frequency-dependent friction of a sphere from hydrodynamic theory

The frequency-dependent friction of a sphere,  $\tilde{\Gamma}^{\text{hyd}}(\omega)$ , is a complex-valued function that describes the fluid stress response to a small, oscillatory sphere motion and is defined as

$$\tilde{F}_i(\omega) = \delta_{ij} \tilde{\Gamma}^{\text{hyd}}(\omega) \tilde{v}_j(\omega), \quad (1)$$

where  $\tilde{v}_j(\omega)$  is the frequency-dependent velocity of the sphere and  $\tilde{F}_i(\omega)$  is an external force acting on the sphere with radius  $a$ , and the indices  $i, j \in \{x, y, z\}$ . In our work, we define the spatial and temporal Fourier transformation (FT) of a function as  $\tilde{f}(\vec{k}, \omega) = \int dt d^3r f(\vec{r}, t) e^{-i(k_r r_i + \omega t)}$ . The friction of a sphere in a liquid can be derived from the Navier-Stokes equation, which originates from local momentum conservation [46–48] and follows as

$$\tilde{\Gamma}^{\text{hyd}}(\omega) = \frac{4\pi \tilde{\eta}(\omega) a}{3} W^{-1} \{ (1 + \hat{\lambda})(9 + 9\hat{\alpha} + \hat{\alpha}^2)(1 + 2\hat{b}) + (1 + \hat{\alpha})[2\hat{\lambda}^2(1 + 2\hat{b}) + \hat{b}\hat{\alpha}^2(1 + \hat{\lambda})] \}, \quad (2)$$

where  $W$  is given by

$$W = (2 + 2\hat{\lambda} + \hat{\lambda}^2)[1 + \hat{b}(3 + \hat{\alpha})] + (1 + \hat{\alpha})(1 + 2\hat{b})\hat{\lambda}^2/\hat{\alpha}^2. \quad (3)$$

Finite slip at the spherical surface is described by the dimensionless slip length  $\hat{b} = b/a$ . The dimensionless constants  $\hat{\alpha} = a\alpha$  and  $\hat{\lambda} = a\lambda$  are defined by

$$\alpha^2(\omega) = i\omega\rho_0/\tilde{\eta}(\omega) \quad (4)$$

and

$$\lambda^2(\omega) = \frac{i\omega\rho_0}{4\tilde{\eta}(\omega)/3 + \tilde{\zeta}(\omega) - i\rho_0 c^2/\omega}, \quad (5)$$

where  $c$  is the speed of sound and  $\rho_0$  is the mean fluid mass density. The full derivation of Eq. (2) is presented in Appendix A.

The shear viscosity  $\tilde{\eta}(\omega)$  and volume viscosity  $\tilde{\zeta}(\omega)$  are defined by the stress tensor in the Navier-Stokes

equation (Appendix A). If the viscous response decays on length- and time-scales that are small compared with those on which the velocity gradients of the fluid  $\nabla_j v_i(\vec{r}, t)$  vary, one can approximate the viscous response as frequency- and momentum-independent, which defines a Newtonian fluid. We consider frequency-dependent and momentum-independent viscosities in this work. The shear viscosity  $\eta(t)$  is calculated from the autocorrelation of the trace-less stress tensor. On the other hand, the volume viscosity  $\zeta(t)$  quantifies a fluid's dissipative response to compression [49] and is crucial for describing processes such as sound propagation or shock waves [35]; it can be calculated from the autocorrelation of instantaneous pressure fluctuations. Often, the volume viscosity is neglected, which corresponds to the Stokes hypothesis [50,51]. However, previous simulations and experiments found that the volume viscosity for water is non-negligible and can even be larger than the shear viscosity [52]. Thus, we explicitly consider a nonvanishing volume viscosity and will carefully examine its influence on the frequency-dependent friction.

### B. Frequency-dependent particle friction from the generalized Langevin equation

For a particle with mass  $m$ , the dynamics can be described by the generalized Langevin equation (GLE) [1,2,9]

$$m\ddot{\vec{r}}(t) = -\vec{\nabla}U[\vec{r}(t)] - \int_{-\infty}^t dt' \Gamma(t-t')\dot{\vec{r}}(t') + \vec{F}_R(t), \quad (6)$$

where  $-\vec{\nabla}U[\vec{r}(t)]$  is the force due to a potential,  $\Gamma(t)$  the friction function, often called the memory kernel, and  $\vec{F}_R(t)$  is the random force, which has zero mean and a variance of

$$\langle F_R^i(t)F_R^j(t') \rangle = k_B T \delta_{ij} \Gamma(|t-t'|), \quad (7)$$

where  $k_B T$  is the thermal energy. The stationary friction coefficient of the particle  $\gamma_0$  is determined by the integral over the memory kernel, i.e.,  $\gamma_0 = \int_0^\infty \Gamma(t)dt$ . We assume isotropic fluids and thus consider only the  $x$  component of the particle position. In the absence of a potential ( $U = 0$ ), the solution of the GLE in Eq. (6) in Fourier space reads for the particle velocity along  $x$  as

$$\tilde{v}_x(\omega) = \frac{\tilde{F}_R(\omega)}{\tilde{\Gamma}_+(\omega) + i\omega m}, \quad (8)$$

where we use the single-sided memory function  $\Gamma_+(t) = \Gamma(t)$  for  $t \geq 0$  and  $\Gamma_+(t) = 0$  for  $t < 0$ . In Appendix B, we show by calculating the fluid momentum outside a moving sphere from the transient Stokes equation that the hydrodynamic friction  $\tilde{\Gamma}^{\text{hyd}}(\omega)$  in Eq. (2) does not include inertial effects inside the sphere. Thus, by comparing Eqs. (1) and (8) we conclude that  $\tilde{\Gamma}^{\text{hyd}}(\omega)$  and  $\tilde{\Gamma}_+(\omega)$  describe the same quantity, namely, the frequency-dependent friction of a particle due to the surrounding fluid.

## III. RESULTS AND DISCUSSION

### A. Frequency-dependent shear and volume viscosities

We analyze MD simulations at temperature  $T = 300$  K for the SPC/E and TIP4P/2005 water models (see Appendix C for simulation details) and compute the frequency-dependent

shear  $\tilde{\eta}(\omega)$  and volume viscosity  $\tilde{\zeta}(\omega)$  (see Appendix D). The Newtonian fluid, as defined in Eq. (A3) in Appendix A, is a standard model to describe large-scale and long-time hydrodynamics of liquid water [47,54,55]. However, in earlier experimental investigations and MD simulations, it was found that, at high frequencies, typically in the THz regime, liquid water deviates from the Newtonian fluid model [32,33,56–64] and that the shear viscosity decreases at high frequencies [36].

In Figs. 1(a)–1(c), we show the extracted shear viscosity in the time and frequency domain from both water models. The TIP4P/2005 model spectra are very similar to the SPC/E model; both exhibit a pronounced peak in the real and imaginary parts around 7–8 THz, which cannot be described by a single-mode relaxation model. We fit the shear viscosity with a sum of six exponential-oscillating functions [36]

$$\eta(t) = \Theta(t) \left\{ \sum_{j=I}^{VI} \frac{\eta_{0,j} \tau_{n,j}}{\tau_{o,j}^2} e^{-t/2\tau_{n,j}} \left[ \frac{1}{\kappa_j} \sin\left(\frac{\kappa_j}{2\tau_{n,j}} t\right) + \cos\left(\frac{\kappa_j}{2\tau_{n,j}} t\right) \right] \right\}, \quad (9)$$

where  $\kappa_j = [4(\tau_{n,j}/\tau_{o,j})^2 - 1]^{1/2}$ , which in the frequency domain reads

$$\tilde{\eta}(\omega) = \sum_{j=I}^{VI} \eta_{0,j} \frac{1 + i\omega\tau_{n,j}}{1 + i\omega\tau_{o,j}^2/\tau_{n,j} - \omega^2\tau_{o,j}^2}, \quad (10)$$

as described in Appendix E. Depending on the value of  $\kappa$ , a viscosity component displays a single-exponential decay with oscillations (finite real part of  $\kappa$ ), or is a sum of two nonoscillating exponentials (imaginary  $\kappa$ ). We find the fit function for both water models to perfectly describe the MD data in Figs. 1(a)–1(c). We provide the fit parameters in Table I in Appendix F, and the individual components for the SPC/E water shear viscosity in Appendix G, all in very good agreement with previous fitting results [36]. The value of the steady-state shear viscosity for the SPC/E model of  $\eta_0 = \sum_j \eta_{0,j} = 0.70$  mPa s is lower than the value  $\eta_0 = 0.84$  mPa s for the TIP4P/2005 model [9,35,65].

Our shear viscosity model decomposes the viscosity spectrum into modes that describe distinct dynamical processes [36]. The slowest nonoscillatory component I is due to hydrogen-bond network topology changes, i.e., changes of nearest-neighbor water pairs, while component II is due to hydrogen-bond bending vibrations of water pairs, they are both overdamped [36]. The large peak around 7 THz is due to the oscillatory component III, which causes the sign changes between 0.04 and 0.1 ps in Fig. 1(a) and describes separation vibrations of hydrogen-bonded water pairs. It agrees in peak frequency with infrared spectroscopy simulation studies [66]. For SPC/E water, we identify the remaining high-frequency modes IV, V, and VI by comparison with absorption spectra of simulated water [63] as librational modes, i.e., rotational vibrations of individual water molecules. The splitting is related to the fact that rotations between the three main water axes are not equivalent.

In Figs. 1(d)–1(f), we show the volume viscosity extracted from the MD data, which we determine from the

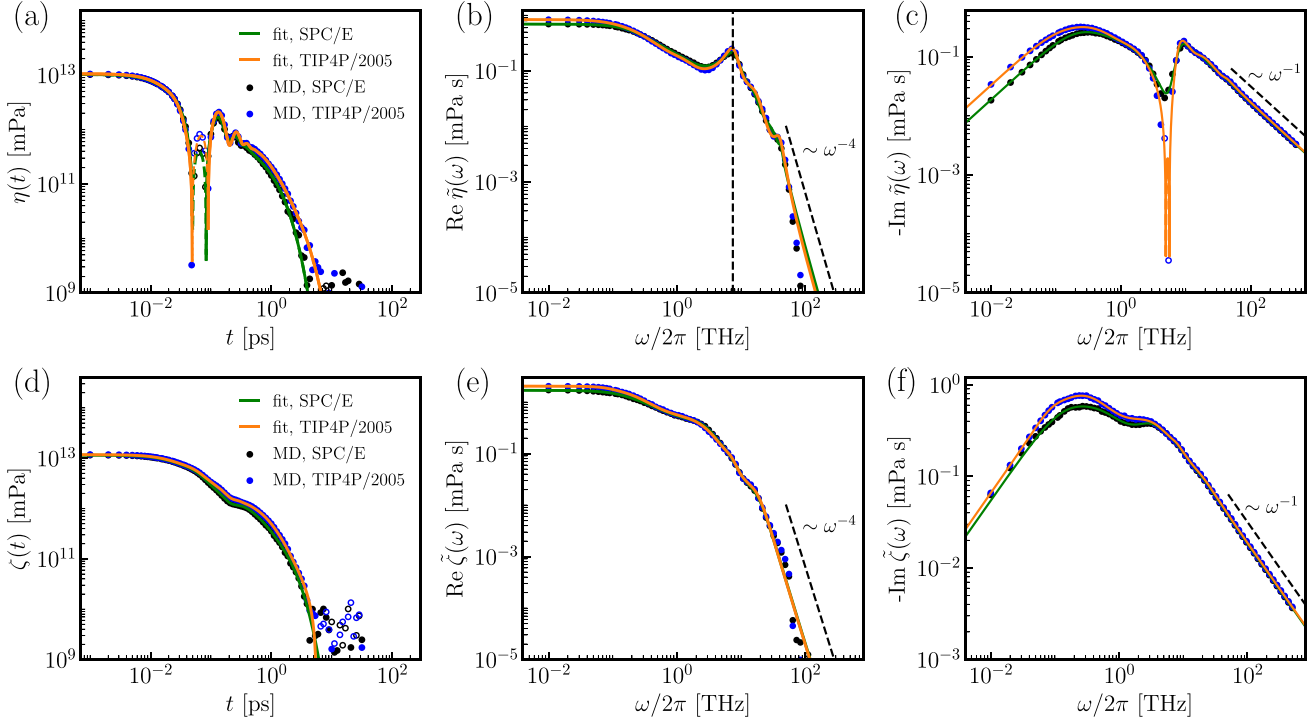


FIG. 1. Extracted shear viscosity  $\eta$  and volume viscosity  $\zeta$  from MD simulations of SPC/E and TIP4P/2005 water. (a) Shear viscosity in the time domain (circles) with fits (lines) according to Eq. (9) and the fitting parameters in Table I (Appendix F). (b), (c) Real and imaginary parts of the shear viscosity in the frequency domain with fits according to Eq. (10). The vertical dashed line denotes the resonance frequency  $f_{r,III} \approx 7.11$  THz from the viscoelastic exponential-oscillatory model. (d) Volume viscosity in the time domain (circles) with fits (lines) according to Eq. (11) and the fitting parameters in Table II (Appendix F). (e), (f) Real and imaginary parts of the volume viscosity in the frequency domain with fits according to Eq. (12). Dashed lines and empty circles denote negative values. Note that all data are shown in logarithmic spacing for better visibility.

autocorrelation of system pressure fluctuations. The real part of these spectra exhibits no distinct peak in the THz regime, contrary to the shear viscosity, and in agreement with previous simulation results [35]. We fit the volume viscosity data with a sum of five exponential-oscillatory components:

$$\zeta(t) = \Theta(t) \left\{ \sum_{j=1}^V \frac{\zeta_{0,j} \tau_{v,j}}{\tau_{w,j}^2} e^{-t/2\tau_{v,j}} \left[ \frac{1}{\kappa_j} \sin\left(\frac{\kappa_j}{2\tau_{v,j}} t\right) + \cos\left(\frac{\kappa_j}{2\tau_{v,j}} t\right) \right] \right\}, \quad (11)$$

where  $\kappa_j = [4(\tau_{v,j}/\tau_{w,j})^2 - 1]^{1/2}$ . The total complex volume viscosity in the frequency domain is given by

$$\tilde{\zeta}(\omega) = \sum_{j=1}^V \zeta_{0,j} \frac{1 + i\omega\tau_{v,j}}{1 + i\omega\tau_{w,j}^2/\tau_{v,j} - \omega^2\tau_{w,j}^2}. \quad (12)$$

The resulting relaxation ( $\tau_{v,j}$ ) and oscillation times ( $\tau_{w,j}$ ), summarized in Table II in Appendix F are rather similar to the shear viscosity fitting results in Table I; this suggests that the components have the same molecular origin as the shear viscosity components I–V.

We find a steady-state value of  $\zeta_0 = \sum_j \zeta_{0,j} = 1.69$  mPa s for the SPC/E, and 2.04 mPa s for the TIP4P/2005 model,

slightly lower than the experimental value (2.4 mPa s for 298 K [52]) and comparable to results from previous MD simulations [35], which yielded for TIP4P/2005 water  $\zeta_0 = 2.07$  mPa s at 298 K and  $\zeta_0 = 2.01$  mPa s at 303 K, and for SPC/E water  $\zeta_0 = 1.57$  mPa s at 298 K and  $\zeta_0 = 1.45$  mPa s at 303 K.

For high frequencies around 100 THz, the fitting functions' real part of both viscosity spectra start to deviate from the MD data, where according to the models in Eqs. (10) and (12) the real part scales as  $\omega^{-4}$  (see dashed black lines). These discrepancies are not a simulation time-step issue (Appendix H) but due to shortcomings of the fitting function [67] and occur at frequencies where intramolecular vibrations of real water take place [63] which are not included in our rigid water models and are not of concern in this work.

## B. Frequency-dependent friction of a sphere from hydrodynamic theory including frequency-dependent viscosities

We insert the shear and volume viscosity spectra from the SPC/E water model MD simulations in Fig. 1 into Eq. (2) to compute the hydrodynamic friction  $\tilde{\Gamma}^{\text{hyd}}(\omega)$  of a sphere. To obtain a feeling for the influence of slip and sphere size, Fig. 2 shows  $\tilde{\Gamma}^{\text{hyd}}(\omega)$  for different values of the sphere radius  $a$  and slip coefficient  $\hat{b} = b/a$  (solid lines). Note that the results are

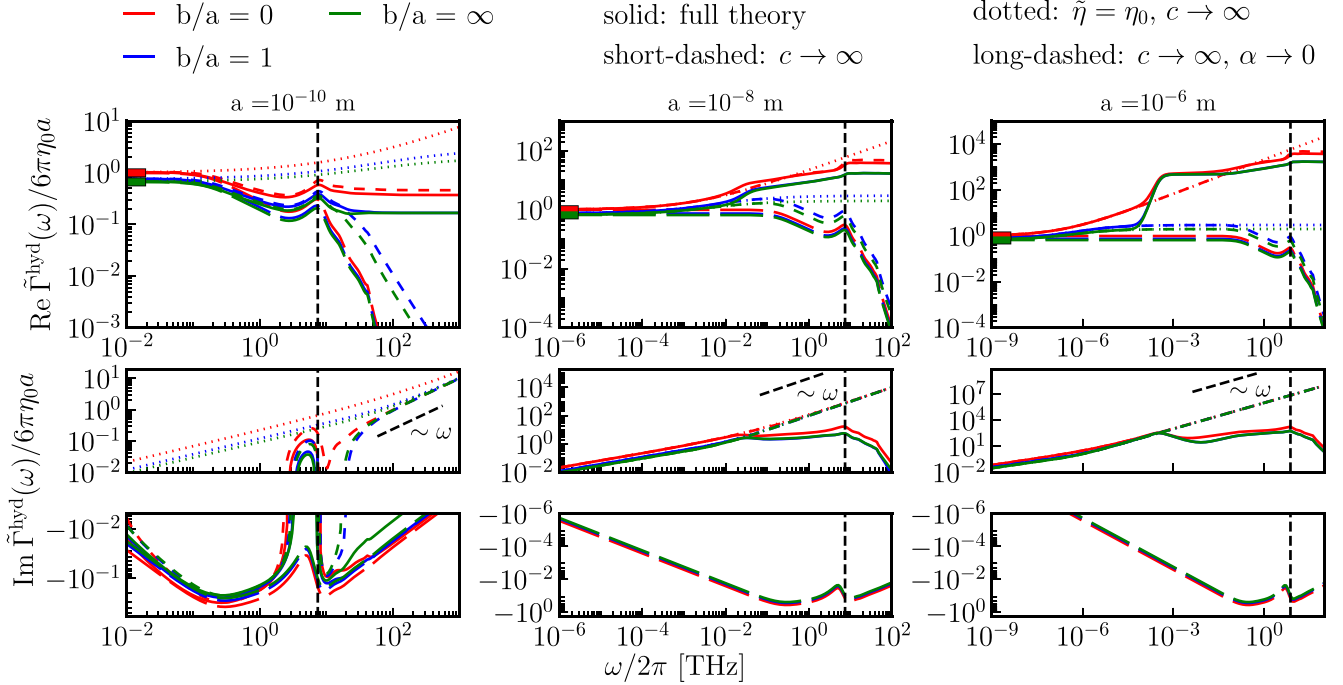


FIG. 2. Real and imaginary parts of the frequency-dependent rescaled friction of a sphere  $\tilde{\Gamma}^{\text{hyd}}(\omega) = \text{Re } \tilde{\Gamma}^{\text{hyd}}(\omega) + i \text{Im } \tilde{\Gamma}^{\text{hyd}}(\omega)$ , given by Eq. (2), for various slip parameters  $\hat{b} = b/a$  and sphere radii  $a$ . Here we use the viscoelastic model for the shear viscosity  $\tilde{\eta}(\omega)$  in Eq. (10) and the volume viscosity  $\tilde{\zeta}(\omega)$  in Eq. (12) for SPC/E water from Fig. 1. The results are normalized by the steady-state viscosity  $\eta_0 = \sum_j \eta_{0,j} = 0.70$  mPa s. We set the water density to  $\rho_0 = 10^3$  kg/m<sup>3</sup> and the speed of sound to  $c = 1.51 \times 10^3$  m/s [53]. The red and green bars to the left denote the  $\omega \rightarrow 0$  limits [46],  $6\pi\eta_0a$  for  $\hat{b} \rightarrow 0$  and  $4\pi\eta_0a$  for  $\hat{b} \rightarrow \infty$ , respectively. We compare the results of the full hydrodynamic theory (solid lines) with the approximation  $c \rightarrow \infty$  (short-dashed lines), which represents the incompressible limit, with the double approximation  $c \rightarrow \infty$  and  $\tilde{\eta} = \eta_0$  (dotted lines), and with the double approximation  $c \rightarrow \infty$  and  $\alpha \rightarrow 0$  (long-dashed lines), which represents the generalized Stokes-Einstein relation [GSER, shown in Eq. (13)]. The vertical dashed line denotes the resonance frequency  $f_{r,III} \approx 7.11$  THz from the viscoelastic exponential-oscillatory model in Fig. 1.

normalized by  $6\pi a\eta_0$  with  $\eta_0 = \sum_j \eta_{0,j} = 0.70$  mPa s, which is the steady-state friction for zero slip. For small radii  $\sim a = 10^{-10}$  m, the friction  $\tilde{\Gamma}^{\text{hyd}}(\omega)$  in Fig. 2 exhibits similar features as the frequency-dependent shear viscosity in Fig. 1 and in particular shows a peak around 7 THz, indicated by vertical dashed lines in Fig. 2. This behavior is absent if a constant shear viscosity is assumed, as shown in Appendix I. The slip length  $b$  has a rather mild effect on the low-frequency friction, as it mostly modulates the absolute value. As  $\omega \rightarrow 0$ , the real part goes to  $6\pi\eta_0a$  for  $\hat{b} \rightarrow 0$  and to  $4\pi\eta_0a$  for  $\hat{b} \rightarrow \infty$  [46], as indicated by horizontal red and green bars to the left in Fig. 2. The real part of the friction functions does not decay to zero as  $\omega \rightarrow \infty$  but instead reaches a plateau, the value of which depends on whether the slip parameter is zero or not. For radii  $a > 10^{-10}$  m, the imaginary part interestingly changes its sign from negative to positive values. In Appendix J, we discuss the asymptotic behavior of the friction function for low and high frequencies. We observe that the imaginary part switches its sign again, which is not visible in the frequency range shown in Fig. 2.

We compare the results with different approximations of the full hydrodynamic theory. Short-dashed lines in Fig. 2 denote the limiting scenario of infinite sound velocity  $c \rightarrow \infty$ , which represents the friction in an incompressible fluid. We observe distinct deviations from the full theory in the real and imaginary parts, which increase with increasing frequency. For  $a = 10^{-10}$  m, compressibility effects at high frequencies

are related to transient density variations originating from the sphere movement, in the form of acoustic waves propagating through the medium [37]. These effects are negligible for low frequencies, as here frequency-dependent viscous effects are dominant. For  $a > 10^{-10}$  m, friction is dominated by compressibility effects that couple to vorticity diffusion [37]. The high-frequency scaling depends strongly on whether we have a finite or a vanishing slip coefficient. Increased slip at the spherical boundary allows the sphere to move more easily through the liquid, resulting in increased compression in front of the sphere, which leads to the subtle coupling between slip and compressibility in Fig. 2.

In the incompressible case, the imaginary part diverges for high frequencies as  $\simeq \rho_0 a^2 \omega / (9\eta_0)$ , corresponding to the so-called added mass term in the force acting on the sphere (see Appendix K for details). This term has been a long-standing issue in literature, since it causes a deviation from the equipartition theorem, i.e.,  $C^{vv}(0) = k_B T / m$ , to  $k_B T / (m + m_0)$ , where  $m_0 = \frac{2}{3}\pi \rho_0 a^3$  is the added mass corresponding to half of the displaced fluid. The added mass term vanishes in the full hydrodynamic theory that includes compressibility, in agreement with previous works [21,27,29,30].

Dotted lines in Fig. 2 denote the incompressible case with a constant shear viscosity, i.e.,  $\tilde{\eta} = \eta_0$ . The friction, in this case, significantly differs from the case of frequency-dependent shear viscosity, in particular the distinct peak around 7 THz is absent. The long-dashed lines represent the case  $c \rightarrow \infty$

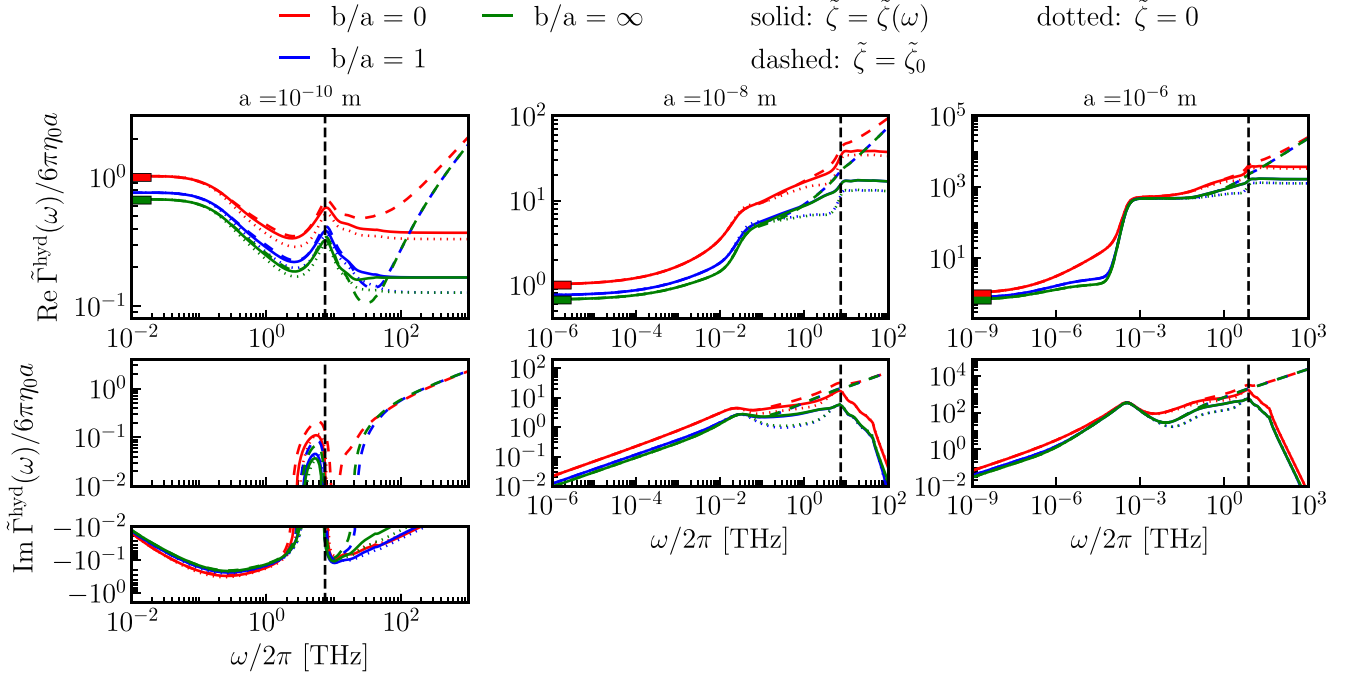


FIG. 3. Investigation of the volume viscosity's influence on the hydrodynamic friction of a sphere  $\tilde{\Gamma}^{\text{hyd}}(\omega) = \text{Re} \tilde{\Gamma}^{\text{hyd}}(\omega) + i \text{Im} \tilde{\Gamma}^{\text{hyd}}(\omega)$ , given by Eq. (2), for various slip parameters  $\hat{b} = b/a$  and sphere radii  $a$ . Here we use the viscoelastic model for the shear viscosity  $\tilde{\eta}(\omega)$  in Eq. (10) for SPC/E water from Fig. 1. The results are normalized by the steady-state viscosity  $\eta_0 = \sum_j \eta_{0,j} = 0.70$  mPa s. We set the water density to  $\rho_0 = 10^3$  kg/m<sup>3</sup> and the speed of sound to  $c = 1.51 \times 10^3$  m/s [53]. We show results for frequency-independent volume viscosity  $\zeta_0 = \sum_j \zeta_{0,j} = 1.69$  mPa s (dashed lines), for vanishing volume viscosity ( $\zeta = 0$ , dotted lines) and for the full frequency-dependent volume viscosity from Fig. 1(d) (solid lines). The red and green bars denote the  $\omega \rightarrow 0$  limits [46],  $6\pi\eta_0 a$  for  $\hat{b} \rightarrow 0$  and  $4\pi\eta_0 a$  for  $\hat{b} \rightarrow \infty$ , respectively. The vertical dashed line denotes the resonance frequency  $f_{r,III} \approx 7.11$  THz from the viscoelastic exponential-oscillatory model in Fig. 1.

and  $\alpha \rightarrow 0$ , where the hydrodynamic friction converges to the so-called generalized Stokes-Einstein relation (GSER),

$$\tilde{\Gamma}^{\text{hyd}}(\omega) = 6\pi\tilde{\eta}(\omega)a \frac{1 + 2\hat{b}}{1 + 3\hat{b}}, \quad (13)$$

which is, in general with the additional approximation  $b \rightarrow 0$ , widely used in the context of rheological theory [45,68,69]. As seen from Eq. (13), the GSER prediction is proportional to the shear viscosity spectra but differs significantly from the full hydrodynamic theory, in particular for large radii and in the high-frequency regime.

In Fig. 3, we analyze the dependence of the hydrodynamic friction on the volume viscosity  $\zeta(\omega)$ . We compare the hydrodynamic friction for a finite frequency-independent volume viscosity  $\zeta_0 = \sum_j \zeta_{0,j} = 1.69$  mPa s (dashed lines), for vanishing volume viscosity  $\zeta_0 = 0$ , corresponding to the Stokes hypothesis (dotted lines) and for the frequency-dependent volume viscosity extracted from MD simulations in Fig. 1 (solid lines). For large frequencies, we see that the real part of the friction diverges for constant volume viscosity but goes to a constant when using the full frequency-dependent volume viscosity from MD simulations or a vanishing volume viscosity (Appendix J). This shows that compression effects dominate the friction at high frequencies if an erroneous constant volume viscosity is assumed. Remarkably, the predicted friction function in the low-frequency regime changes only marginally if, instead of the full frequency-dependent volume viscosity, a

vanishing volume viscosity is assumed, demonstrating that the Stokes assumption [50], i.e., the neglect of volume viscosities, is a very accurate approximation. However, the deviation between both scenarios increases for higher frequencies.

### C. Comparison of the hydrodynamic and GLE friction for water and the hydrodynamic tail

In the following, we compare the friction function  $\Gamma(t)$ , defined by the GLE in Eq. (6) and extracted from the MD simulations for SPC/E water (Appendix L) with the hydrodynamic prediction. In Figs. 4(a) and 4(b) we compare the real and imaginary parts of  $\tilde{\Gamma}_+(\omega)$  from the GLE (circles) with predictions from the hydrodynamic Eq. (2) using different approximations: the green line shows  $\tilde{\Gamma}^{\text{hyd}}(\omega)$  using the frequency-dependent shear and volume viscosities extracted from MD simulations, the yellow line shows  $\tilde{\Gamma}^{\text{hyd}}(\omega)$  using the frequency-dependent shear viscosity  $\tilde{\eta}(\omega)$  but neglecting compressibility, i.e.,  $c \rightarrow \infty$ , and shear-wave effects, i.e.,  $\alpha \rightarrow 0$ , which corresponds to the GSER in Eq. (13), the blue line shows the hydrodynamic friction using a Maxwell model for the shear viscosity, i.e.,  $\tilde{\eta}(\omega) = \eta_0/(1 + i\omega\tau)$  and vanishing volume viscosity  $\zeta = 0$ . We compare the bare MD result for the memory kernel (red circles) with the result obtained by subtracting the effect of periodic boundary conditions (PBCs) [44] (black circles, Appendix M). Note that here we show results from an MD simulation of SPC/E water with extended trajectory length compared to the results shown in Fig. 1

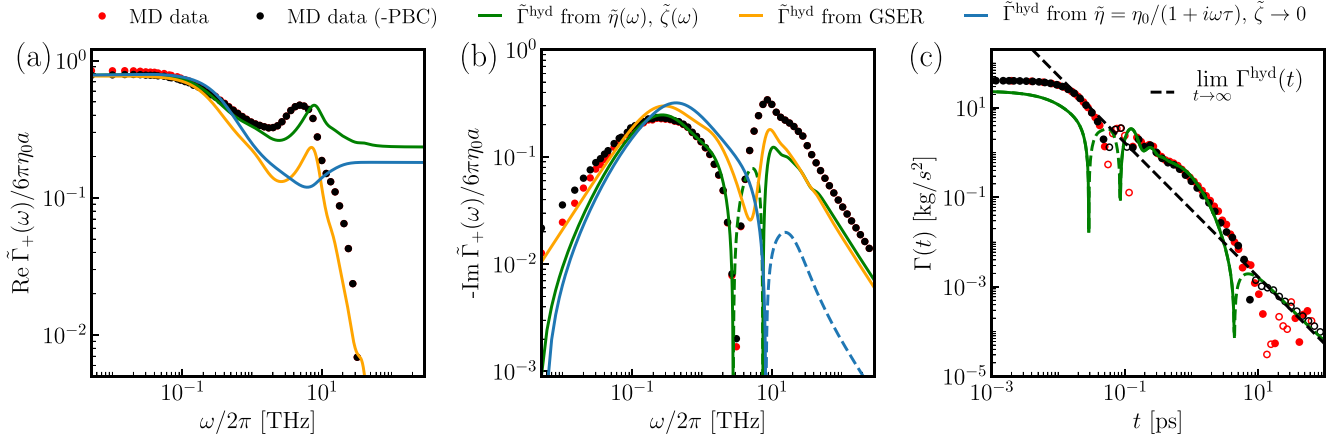


FIG. 4. Comparison between the frequency-dependent friction of a SPC/E water molecule from the GLE,  $\tilde{\Gamma}_+(\omega)$  (circles) and the hydrodynamic prediction,  $\tilde{\Gamma}^{\text{hyd}}(\omega)$  (lines). (a), (b) Real and imaginary part of the Fourier transformed friction  $\tilde{\Gamma}_+(\omega)$  extracted from MD simulations (see Appendix L for details). The red and black circles denote the MD results without and with finite-size correction (Appendix M), respectively. We compute  $\tilde{\Gamma}^{\text{hyd}}(\omega)$  according to Eq. (2) (green) for  $a = 0.14$  nm and  $\hat{b} = b/a = 0.72$  and using the shear and volume viscosity parameters given in Appendix F. For the yellow lines we neglect compressibility, i.e.,  $c \rightarrow \infty$ , and shear wave effects, i.e.,  $\alpha \rightarrow 0$ , which corresponds to the GSER in Eq. (13). The blue lines show the hydrodynamic friction using a Maxwell model fit of the shear viscosity to the MD friction data and vanishing volume viscosity  $\tilde{\zeta} = 0$ . The fitting constants are  $\eta_0 = 0.70$  mPa s and  $(2\pi\tau)^{-1} = 0.43$  THz. (c) Time-domain behavior of the water friction function in panels (a) and (b). We compare the MD data (circles) with the numerical inverse Fourier transformation of the hydrodynamic friction  $\tilde{\Gamma}^{\text{hyd}}(\omega)$  in Eq. (2) (green). The black dashed line is the predicted hydrodynamic tail in Eq. (15). Dashed lines and empty circles denote negative values. The MD data for times higher than 10 ps are smoothed to reduce numerical noise.

(Appendix C), for the purpose of reducing statistical noise in the long-time behavior.

The friction  $\tilde{\Gamma}_+(\omega)$  exhibits the same features as the hydrodynamic prediction  $\tilde{\Gamma}^{\text{hyd}}(\omega)$  from Eq. (2) (green), especially a peak around 6–8 THz that is slightly shifted to higher frequencies in the hydrodynamic prediction. Here, we use  $a = 0.14$  nm and  $\hat{b} = 0.72$ , which we obtain from fitting to the MD results in the frequency domain, as described in Appendix N. The prediction using the full frequency-dependent shear and volume viscosities (green) agrees rather nicely with the friction directly extracted from the GLE. Deviations between the MD data and the green lines become noticeable for frequencies above 10 THz, where in the real part the hydrodynamic prediction converges to a plateau while the MD data decay to zero. These deviations are not unexpected [30] since standard hydrodynamic theory can not correctly describe the local interaction of the sphere with its environment for high frequencies, which are mediated by smooth intermolecular forces [67,70] that are not described accurately by an abrupt boundary condition at the spherical surface. Thus, we find that the friction can be predicted well by continuous hydrodynamic theory including complex shear and volume viscosity models below a frequency of 10 THz. The shear viscosity spectrum gives rise to the resonant feature in the friction kernel  $\tilde{\Gamma}_+(\omega)$  around 7 THz, which is missed by the Maxwell model used in previous theoretical models (blue line) [30,31].

The residual discrepancies below 10 THz could be caused by a modified viscosity near the particle surface since a hydration shell cannot be expected to be characterized by the macroscopic shear viscosity. In Appendix O, we show that good agreement between hydrodynamic theory and MD is

also obtained for a simpler system such as a Lennard-Jones fluid.

Interestingly, the good agreement for the low-frequency behavior in the friction function assumes non-negligible slip  $b \neq 0$ . In Appendix N, we discuss the influence of the radius  $a$  and the slip length  $b$  on the hydrodynamic friction. The fitted values we obtain for the sphere radius  $a = 0.14$  nm and the slip length  $b = 0.10$  nm (Appendix N) are in a realistic range around 1 Å. We obtain a water molecule mass of  $m \approx 3 \times 10^{-26}$  kg from the equipartition theorem  $mC^{vv}(0) = k_B T$ . For a density of  $\rho_0 \approx 10^3$  kg/m<sup>3</sup>, the estimate of the hydrodynamic radius using  $m = \frac{4}{3}\pi\rho_0 a^3$  is  $a \approx 0.19$  nm, in rough agreement with the fitted hydrodynamic radius. In fact, our estimated radius and slip length are comparable with independent results  $a \approx 0.15$  nm and  $b \approx 0.10$  nm obtained from translational and rotational diffusion constants for SPC/E water [38].

In an unbounded fluid, hydrodynamic backflow effects lead for long times to a power-law decay of the memory kernel as  $\lim_{t \rightarrow \infty} \Gamma^{\text{hyd}}(t) \approx -3a^2 \sqrt{\pi\eta_0\rho_0} t^{-3/2}$  [20,71,72], which follows from our expression of the hydrodynamic friction in Eq. (2) by neglecting slip, i.e.,  $b \rightarrow 0$ , and vanishing compressibility, i.e.,  $c \rightarrow \infty$  (Appendix K). However, previous MD simulations of solute particles in liquid environments [8,67] did not observe the predicted tail, rather showing a positive sign or a different power-law behavior. Here we use hydrodynamic theory and finite-size effects to explain the absence of the tail in simulations, the influence of compressibility, slip, and frequency-dependent viscosity on the hydrodynamic tail has already been discussed in Ref. [26]. Since, as we show in Appendix P, compressibility does not influence the hydrodynamic tail but is only relevant on

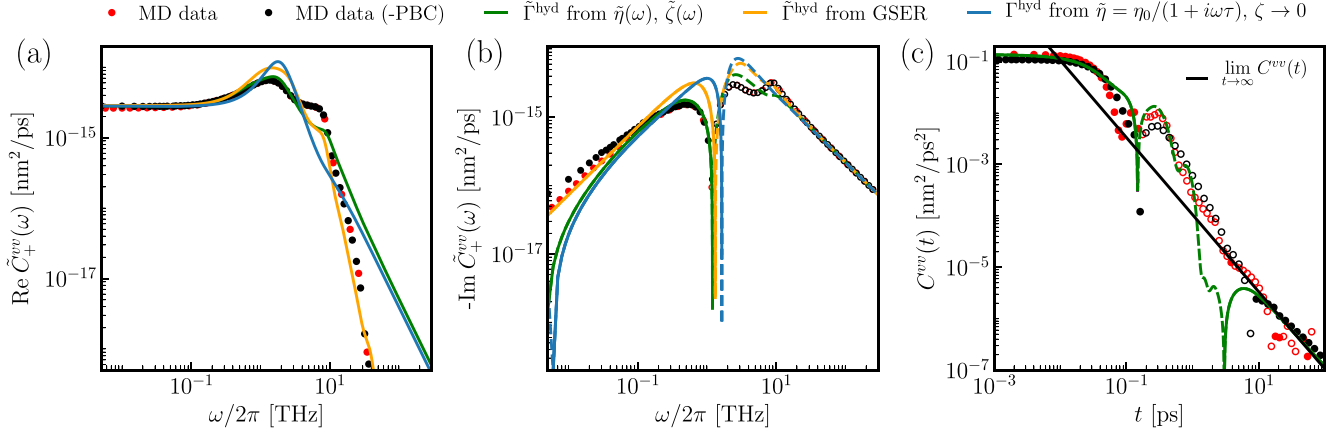


FIG. 5. Comparison between the frequency-dependent velocity autocorrelation function  $\tilde{C}_+^{vv}(\omega)$  of a water molecule in water from MD simulations (circles) with the hydrodynamic prediction according to Eq. (16), using the results  $\tilde{\Gamma}_+(\omega)$  from hydrodynamic theory shown in Fig. 4. The color coding is the same as in Fig. 4. The black line in panel (c) is the predicted hydrodynamic tail in Eq. (17).

intermediate time scales, we assume  $\lambda \rightarrow 0$  in Eq. (2). As shown in Appendix J, for low frequencies the hydrodynamic memory kernel in Eq. (2) can be expanded as

$$\frac{\tilde{\Gamma}^{\text{hyd}}(\omega)}{6\pi\eta_0 a} \simeq \frac{1+2\hat{b}}{1+3\hat{b}} + \frac{a(1+2\hat{b})^2\sqrt{i\omega\rho_0/\eta_0}}{\sqrt{2}(1+3\hat{b})^2} + O(\omega^{3/2}). \quad (14)$$

We see that the  $\omega^{1/2}$  term, which is responsible for the  $t^{-3/2}$  power-law decay, depends on the slip length  $\hat{b}$ . Higher-order terms are influenced by the slip length  $b$  and the model we choose for the shear viscosity  $\tilde{\eta}(\omega)$ . By inverse Fourier transformation, one obtains for long times

$$\lim_{t \rightarrow \infty} \Gamma^{\text{hyd}}(t) \approx -3a^2 \frac{(1+2\hat{b})^2}{(1+3\hat{b})^2} \sqrt{\pi\eta_0\rho_0} t^{-3/2}, \quad (15)$$

whose absolute values are shown as a black dashed line in Fig. 4(c). The long-time behavior of the water memory kernel is governed by a competition between the hydrodynamic tail and the long-time behavior of the frequency-dependent shear viscosity we use. The power-law tail in the MD data agrees perfectly with Eq. (15) if we subtract the masking finite-size effects (black circles). The uncorrected MD data (red circles) are dominated by PBC effects and do not exhibit the long-time tail in Eq. (15) at time scales reachable with MD simulations [44].

#### D. Long-time tail of the velocity autocorrelation function

The velocity autocorrelation function  $C^{vv}(t)$  (VACF) of a solute particle was used in various studies to compare hydrodynamic and stochastic theories [27,29–31]. The GLE in Eq. (6) relates the memory kernel and the VACF by a Volterra equation (Appendix L), which in the Fourier domain can be written as (derived in Appendix Q)

$$\tilde{C}_+^{vv}(\omega) = \frac{i\omega k_B T}{i\omega\tilde{\Gamma}_+(\omega) - m\omega^2}. \quad (16)$$

In Fig. 5, we compare predictions according to Eq. (16) using hydrodynamic theory with MD results for the VACF. As for the memory kernel, we achieve good agreement in the fre-

quency domain up to frequencies of 10 THz with the full theory in Eq. (2) (green line). The hydrodynamic tail of the VACF for long times (Appendix K)

$$\lim_{t \rightarrow \infty} C^{vv}(t) \approx \frac{k_B T \sqrt{\rho_0}}{12} (\pi\eta_0 t)^{-3/2}, \quad (17)$$

agrees with the prediction from hydrodynamic theory and the MD data when applying the finite-size correction (black circles) for long times  $> 10$  ps in Fig. 5(c). These findings for the VACF support that the best prediction of molecular water dynamics is achieved by including the macroscopic viscosity spectra of water into the hydrodynamic theory.

#### E. Results for a methane molecule moving in water

In Fig. 6 we show the memory kernel  $\tilde{\Gamma}_+(\omega)$  for a single methane molecule in SPC/E water extracted from MD simulations, again with and without PBC and finite-size correction. The data are taken from the work of Kowalik *et al.* [9]. The methane molecule in these simulations is modeled as a monoatomic Lennard-Jones sphere, which makes it possible to compute the friction using Eq. (2) for a spherical particle. In Figs. 6(a) and 6(b), we see that the real and imaginary parts of the Fourier transformed friction  $\tilde{\Gamma}_+(\omega)$  do not show the same features as the prediction from the hydrodynamic equations (green and yellow), even when we freely adjust the radius  $a$  and the slip coefficient  $\hat{b}$ . In particular, the pronounced peak in the real part at around 7–8 THz arising from the shear viscosity of water is absent in the MD data, and the MD memory kernel in the time domain in Fig. 6(c) does not contain any noticeable oscillations, in contrast to the hydrodynamic prediction.

Thus, we observe considerable discrepancies between the friction extracted directly from MD simulations and the hydrodynamic prediction for a hydrophobic molecule in a water environment. Slip effects on the methane surface cannot explain these differences. Rather, the local shear viscosity near the methane molecule seems to differ from the bulk shear viscosity. This is in line with a recent analysis of tracer-particle dynamics in hydrogels, where the assumption of a thin interfacial shell with viscoelastic properties different from

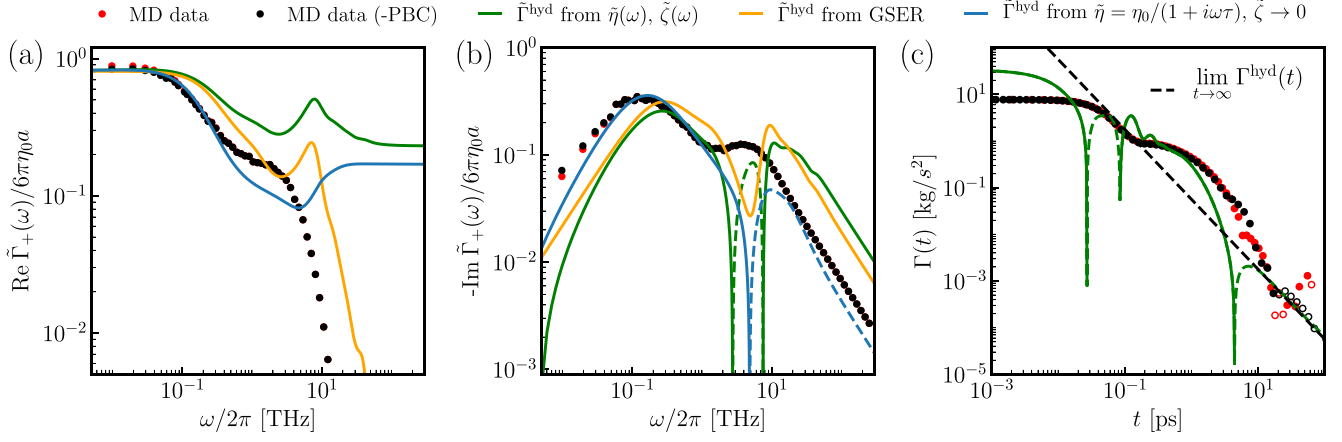


FIG. 6. Comparison between the frequency-dependent friction of a single methane molecule in water extracted from MD simulations using the GLE in Eq. (6) and the hydrodynamic prediction in Eq. (2). (a), (b) Real and imaginary part of the Fourier transformed friction  $\tilde{\Gamma}_+(\omega)$  (time resolution 2 fs, data from Ref. [9]). The red and black circles denote the MD results without and with finite-size correction (Appendix M), respectively. We compare the computed friction with the results from Eq. (2) (green) for  $a = 0.14$  nm and  $\hat{b} = b/a = 0.45$  and the shear and volume viscosity parameters given in Appendix F. The yellow line corresponds to the GSER in Eq. (13). The blue line shows the hydrodynamic friction using a Maxwell model fit of the shear viscosity to the MD friction data and vanishing volume viscosity  $\tilde{\zeta} = 0$ . The fitting constants are  $\eta_0 = 0.70$  mPa s and  $(2\pi\tau)^{-1} = 0.17$  THz. (c) Time domain behavior of the methane memory kernel in panels (a) and (b). We compare the MD data (circles) with the numerical inverse Fourier transformation of the full hydrodynamic friction  $\tilde{\Gamma}^{\text{hyd}}(\omega)$  in Eq. (2). The black dashed line is the predicted hydrodynamic tail in Eq. (15).

bulk reconciles the experimental measurements with hydrodynamic predictions [45].

#### F. Frequency-dependent surface slip from MD simulations

The observation that the full hydrodynamic theory for a water and a methane molecule does not accurately predict the friction kernels extracted directly from the MD data above 10 THz in Figs. 4 and 6, and that better agreement in this frequency range is rather achieved with the much simpler GSER model, is a clear sign that the hydrodynamic theory used by us misses key aspects of molecular friction. A reasonable extension is to assume the slip coefficient  $b$ , which follows from the Navier boundary condition at the spherical

surface (Appendix A), to be frequency-dependent as well, i.e.,  $b = \tilde{b}(\omega)$ . Note that a frequency-dependent surface friction coefficient, i.e.,  $\tilde{\Lambda}(\omega) = \tilde{\eta}(\omega)/\tilde{b}(\omega)$ , has been introduced in a few previous works [73–75]. To obtain the slip spectrum, we assume the frequency-dependent memory kernel  $\tilde{\Gamma}_+(\omega)$  to equal the hydrodynamic expression in Eq. (2) and solve for the slip length  $\tilde{b}(\omega)$ . The results for the slip spectra in Fig. 7 for different radii  $a$  by construction lead to a perfect agreement between the friction from the MD data in Figs. 4 and 6 and the hydrodynamic prediction and exhibit interesting features. In particular, we observe regions where the real part of the slip coefficient is negative, which would correspond to a negative real part of the surface friction coefficient  $\tilde{\Lambda}(\omega)$ , contrary to standard models. Negative slip coefficients indicate a local

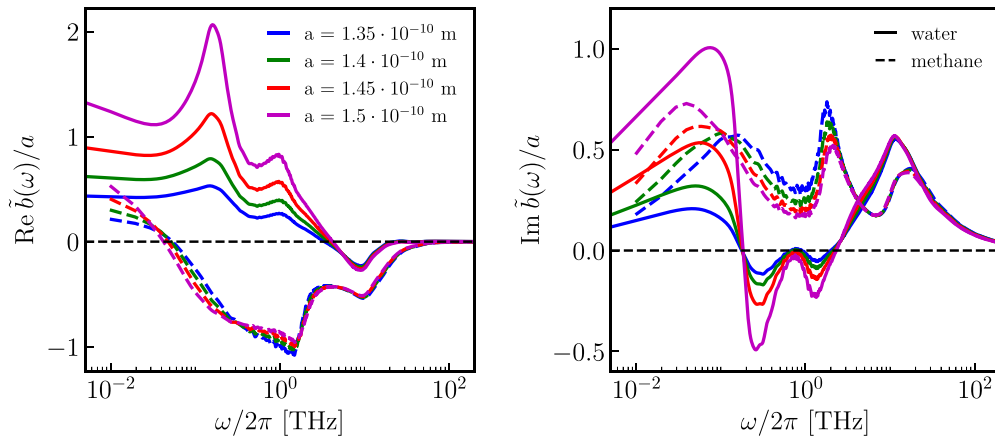


FIG. 7. Frequency-dependent slip length  $\tilde{b}(\omega) = \text{Re } \tilde{b}(\omega) + i \text{Im } \tilde{b}(\omega)$  obtained by assuming the frequency-dependent friction kernel  $\tilde{\Gamma}_+(\omega)$  extracted from MD data shown in Figs. 4 and 6 to be equivalent to the hydrodynamic expression in Eq. (2) and solving the equation for the slip length  $\tilde{b}(\omega)$ . We show predictions for different radii  $a$ . Solid lines denote results for water and dashed lines for methane.

shear viscosity around the spherical particle that is higher than the bulk viscosity [76].

For the molecular water friction, denoted by solid lines, a distinct positive peak in the real part around 0.2 THz is visible, which is in the region of the shear viscosity mode I of water (Appendix F) and relates to an induced slip effect due to hydrogen network topology changes. The real part of the slip length of a water molecule at the prominent peak of shear viscosity mode III around 7–8 THz is negative, suggesting that hydrogen stretching modes cause a local viscosity around a water molecule higher than the macroscopic shear viscosity. For methane, denoted by dashed lines in Fig. 7, the real part is negative in nearly the entire frequency range. This agrees with the fact that methane in water is surrounded by a highly-ordered solvation and presumably highly viscous shell structure [8].

#### IV. CONCLUSIONS

We demonstrate that predictions from continuous hydrodynamic theory for a sphere are in good agreement with the friction coefficient directly extracted via the GLE from MD simulations of a single water molecule in liquid water if the frequency dependence of the macroscopic shear and volume viscosities is properly accounted for, and the hydrodynamic radius and the slip coefficient are used as fitting parameters. This establishes the long-sought link between macroscopic fluid hydrodynamics and the molecular friction in a fluid. We also show that it is important to include the frequency-dependent volume viscosity of the fluid which asymptotically decays as  $\tilde{\zeta} \rightarrow 0$  for  $\omega \rightarrow \infty$ .

Interestingly, good agreement between the molecular water friction (obtained via the GLE) and the hydrodynamic prediction is achieved without including spatial or wave-vector dependencies of the viscosities, which certainly are present [56] and can be modeled by Burnett theory [77,78]. We have mostly dealt with the homogeneous case, where the moving molecule is identical to the surrounding fluid molecules. In contrast, we observe pronounced discrepancies between the friction obtained from hydrodynamic theory and simulations for the inhomogeneous case of a methane molecule moving in water. By calculating the frequency-dependent surface slip from the comparison of MD simulation results and hydrodynamic prediction, we conclude that our hydrodynamic model neglects the modified viscous properties of the water solvation layer around a methane molecule. It would therefore be desirable to develop inhomogeneous hydrodynamic models for the friction of host molecules in liquids in the presence of solvation shells that exhibit viscosity properties different from the bulk.

#### ACKNOWLEDGMENTS

This work was supported by the Deutsche Forschungsgemeinschaft (DFG) via Grant No. SFB 1449 Project Id 431232613 “Dynamic Hydrogels at Biointerfaces,” Project A02, and Grant No. SFB 1114 Project Id 235221301 “Scaling Cascades in Complex Systems,” Project C02. The authors would like to acknowledge the HPC Service of ZEDAT, Freie Universität Berlin, for providing computing time.

#### APPENDIX A: HYDRODYNAMIC FRICTION OF A SPHERE FROM THE TRANSIENT STOKES EQUATION

The Navier-Stokes equation reads

$$\frac{\partial \rho(\vec{r}, t) v_i(\vec{r}, t)}{\partial t} + \nabla_j \rho(\vec{r}, t) v_i(\vec{r}, t) v_j(\vec{r}, t) = F_i(\vec{r}, t) + \nabla_j \sigma_{ij}(\vec{r}, t), \quad (\text{A1})$$

where  $i, j \in \{x, y, z\}$  and doubly appearing indices are summed over. The mass density  $\rho$ , velocity  $v_i$  and volume force  $F_i$  are functions of time  $t$  and position  $\vec{r}$ . The symmetric stress tensor  $\sigma_{ij}(\vec{r}, t)$  consists of a diagonal pressure contribution and components that depend on velocity gradients,  $\nabla_j v_i(\vec{r}, t)$  [36,41,79,80]. For a linear, homogeneous, isotropic compressible fluid, it is on the linear level given by

$$\begin{aligned} \sigma_{ij}(\vec{r}, t) = & -P(\vec{r}, t) \delta_{ij} + \iint \left[ \eta(|\vec{r}'|, t') (\nabla_i v_j(\vec{r} - \vec{r}', t - t') \right. \\ & + \nabla_j v_i(\vec{r} - \vec{r}', t - t')) \\ & + \delta_{ij} \left( \zeta(|\vec{r}'|, t') - \frac{2}{3} \eta(|\vec{r}'|, t') \right) \\ & \left. \times \nabla_k v_k(\vec{r} - \vec{r}', t - t') \right] d\vec{r}' dt', \quad (\text{A2}) \end{aligned}$$

where  $P$  is the pressure and  $\eta$  and  $\zeta$  are the shear and volume viscosity kernels, which in general are time- and space-dependent. If the viscosity kernels decay on length- and timescales that are small compared to those on which  $\nabla_j v_i(\vec{r}, t)$  varies, one can approximate the stress tensor in Eq. (A2) as

$$\begin{aligned} \sigma_{ij}(\vec{r}, t) \approx & -P(\vec{r}, t) \delta_{ij} + \left( \zeta_0 - \frac{2}{3} \eta_0 \right) \delta_{ij} \nabla_k v_k(\vec{r}, t) \\ & + \eta_0 (\nabla_i v_j(\vec{r}, t) + \nabla_j v_i(\vec{r}, t)), \quad (\text{A3}) \end{aligned}$$

where  $\eta_0$  and  $\zeta_0$  are the time- and space-integrated viscosities:

$$\eta_0 = \iint \eta(|\vec{r}'|, t') d\vec{r}' dt', \quad (\text{A4})$$

$$\zeta_0 = \iint \zeta(|\vec{r}'|, t') d\vec{r}' dt'. \quad (\text{A5})$$

A fluid with a stress tensor given by Eq. (A3) is called a Newtonian fluid, here the viscosities are time- and space-independent and the stress tensor is linear in the velocity gradients. In this work, we consider viscoelastic fluids for which the viscosity depends on the history of the velocity gradients. If we neglect the nonlinear term in the Navier-Stokes equation [second term on the left-hand side in Eq. (A1)], which is justified for low Reynolds numbers, and use the expression of the stress tensor in Eq. (A2), we arrive at the linear transient Stokes equation

$$\begin{aligned} \rho(\vec{r}, t) \frac{\partial v_i(\vec{r}, t)}{\partial t} = & F_i(\vec{r}, t) - \nabla_i P(\vec{r}, t) + \iint \left( \frac{1}{3} \eta(|\vec{r}'|, t') + \zeta(|\vec{r}'|, t') \right) \\ & \times \nabla_i \nabla_k v_k(\vec{r} - \vec{r}', t - t') d\vec{r}' dt' \\ & + \iint \eta(|\vec{r}'|, t') \nabla_k \nabla_k v_i(\vec{r} - \vec{r}', t - t') d\vec{r}' dt'. \quad (\text{A6}) \end{aligned}$$

The frequency-dependent friction of a sphere can be calculated using the Green's function of the Stokes equation in Eq. (A6) [37,48]. To derive the Green's function, we take the divergence of Eq. (A6) and obtain

$$\begin{aligned} \nabla_i^2 P(\vec{r}, t) - \frac{\partial^2 P(\vec{r}, t)}{c^2 \partial t^2} \\ = \nabla_i F_i(\vec{r}, t) + \iint \left( \frac{4}{3} \eta(|\vec{r}'|, t') + \zeta(|\vec{r}'|, t') \right) \\ \times \nabla_i^2 \nabla_k v_k(\vec{r} - \vec{r}', t - t') d\vec{r}' dt', \end{aligned} \quad (\text{A7})$$

where we used the linearized continuity equation, i.e.,  $\rho_0 \nabla_i (\partial v_i / \partial t) = -\partial^2 \rho / \partial t^2$ , and the linearized isentropic equation of state  $\rho - \rho_0 = c^{-2}(P - P_0)$ , where the speed of sound is denoted by  $c$ , from which follows that  $\partial^2 \rho / \partial t^2 = c^{-2} \partial^2 P / \partial t^2$ . Fourier-transforming Eqs. (A6) and (A7), we obtain

$$\begin{aligned} i\omega \rho_0 \tilde{v}_i(\vec{k}, \omega) = \tilde{F}_i(\vec{k}, \omega) - ik_i \tilde{P}(\vec{k}, \omega) \\ - [\tilde{\eta}(\vec{k}, \omega)/3 + \tilde{\zeta}(\vec{k}, \omega)] k_i k_j \tilde{v}_j(\vec{k}, \omega) \\ - \tilde{\eta}(\vec{k}, \omega) k_j k_j \tilde{v}_i(\vec{k}, \omega), \end{aligned} \quad (\text{A8})$$

and

$$\begin{aligned} \left( \frac{\omega^2}{c^2} - k_i k_i \right) \tilde{P}(\vec{k}, \omega) \\ = ik_i \tilde{F}_i(\vec{k}, \omega) - i[4\tilde{\eta}(\vec{k}, \omega)/3 + \tilde{\zeta}(\vec{k}, \omega)] k_i k_j \tilde{v}_j(\vec{k}, \omega). \end{aligned} \quad (\text{A9})$$

Note that the viscosity kernels  $\eta$  and  $\zeta$  are both single-sided in the time domain, i.e.,  $\eta(\vec{r}, t) = 0$  and  $\zeta(\vec{r}, t) = 0$  for  $t < 0$ . We next assume that both viscosities decay quickly in space, so that their Fourier transforms become independent of  $k$ , i.e.,  $\tilde{\eta}(\vec{k}, \omega) \rightarrow \tilde{\eta}(\omega)$  and  $\tilde{\zeta}(\vec{k}, \omega) \rightarrow \tilde{\zeta}(\omega)$ . Solving Eq. (A9) for  $\tilde{P}$  and inserting into Eq. (A8), we arrive at an equation for the velocity as a function of the external force [37]. To solve this equation, we decompose the velocity into the transverse and longitudinal parts, i.e.,  $\tilde{v}_i(\vec{k}, \omega) = \tilde{v}_i^T(\vec{k}, \omega) + \tilde{v}_i^L(\vec{k}, \omega)$ , which fulfill  $k_i \tilde{v}_i^T(\vec{k}, \omega) = 0$  and  $k_i \tilde{v}_i^L(\vec{k}, \omega) = k_i \tilde{v}_i^L(\vec{k}, \omega)$ . In Fourier space, the Green's function  $\tilde{G}_{ij}$  of the velocity is defined by

$$\tilde{v}_i(\vec{k}, \omega) = \tilde{G}_{ij}(\vec{k}, \omega) \tilde{F}_j(\vec{k}, \omega) \quad (\text{A10})$$

and is a sum of transverse and longitudinal components, i.e.,  $\tilde{G}_{ij}(\vec{k}, \omega) = \tilde{G}_{ij}^T(\vec{k}, \omega) + \tilde{G}_{ij}^L(\vec{k}, \omega)$ . The transverse part describes the velocity field in the incompressible case and accounts for shear effects. It is given by

$$\tilde{G}_{ij}^T(\vec{k}, \omega) = \frac{(\delta_{ij} - k_i k_j / k^2) / \tilde{\eta}(\omega)}{k^2 + \alpha^2(\omega)}, \quad (\text{A11})$$

where the length scale  $\alpha^{-1}$  is defined as

$$\alpha^2(\omega) = i\omega \rho_0 / \tilde{\eta}(\omega). \quad (\text{A12})$$

The longitudinal component describes compression effects and reads

$$\tilde{G}_{ij}^L(\vec{k}, \omega) = \frac{k_i k_j \lambda^2(\omega)}{\tilde{\eta}(\omega) \alpha^2(\omega) k^2 [k^2 + \lambda^2(\omega)]}. \quad (\text{A13})$$

The length scale  $\lambda^{-1}$  is defined as

$$\lambda^2(\omega) = \frac{i\omega \rho_0}{4\tilde{\eta}(\omega)/3 + \tilde{\zeta}(\omega) - i\rho_0 c^2 / \omega}. \quad (\text{A14})$$

The full frequency-dependent Green's function  $G_{ij}(\vec{r}, \omega) = G_{ij}^T(\vec{r}, \omega) + G_{ij}^L(\vec{r}, \omega)$  in real space reads

$$\begin{aligned} G_{ij}(\vec{r}, \omega) = \frac{1}{4\pi \tilde{\eta} \alpha^2 r^3} \{ \delta_{ij} ([1 + r\alpha + r^2 \alpha^2] e^{-r\alpha} \\ - [1 + r\lambda] e^{-r\lambda}) - 3\hat{r}_i \hat{r}_j ([1 + r\alpha + r^2 \alpha^2 / 3] e^{-r\alpha} \\ - [1 + r\lambda + r^2 \lambda^2 / 3] e^{-r\lambda}) \}. \end{aligned} \quad (\text{A15})$$

The asymptotic behavior of the Green's function, which is discussed in detail in Ref. [37], strongly depends on the inverse length scales  $\alpha = \alpha(\omega)$  and  $\lambda = \lambda(\omega)$ . Note that in Ref. [37] a different definition of the Fourier transformation is used and frequency-independent viscosities are assumed.

To calculate the friction acting on an oscillating sphere, we have to compute the Green's function for the stress tensor, denoted by  $\sigma_{ijk}$ , defined as

$$\sigma_{ij}(\vec{r}, \omega) = \sigma_{ijk}(\vec{r}, \omega) F_k(\vec{r}, \omega). \quad (\text{A16})$$

Without derivation and referring to Ref. [37], the stress tensor Green's function is given by

$$\begin{aligned} \sigma_{ijk}(\vec{r}, \omega) / \tilde{\eta}(\omega) = G_{ijk}(\vec{r}, \omega) + G_{jik}(\vec{r}, \omega) \\ + (\alpha^2 / \lambda^2 - 2) G_{llk}(\vec{r}, \omega) \delta_{ij}, \end{aligned} \quad (\text{A17})$$

where  $\nabla_k G_{ij} = G_{kij}$ . To obtain the fluid velocity around a sphere with radius  $a$ , we use the singularity ansatz [48]

$$\tilde{v}_i^{\text{SP}}(\vec{r}, \omega) = (C_0 + C_2 a^2 \nabla_k \nabla_k) G_{ij}(\vec{r}, \omega) \tilde{F}_j(\omega), \quad (\text{A18})$$

which defines the sphere Green's function

$$G_{ij}^{\text{SP}}(\vec{r}, \omega) = (C_0 + C_2 a^2 \nabla_k \nabla_k) G_{ij}(\vec{r}, \omega), \quad (\text{A19})$$

and the velocity field around the sphere follows as  $\tilde{v}_i^{\text{SP}}(\vec{r}, \omega) = \tilde{F}_j(\omega) G_{ij}^{\text{SP}}(\vec{r}, \omega)$ , with  $\tilde{F}_j$  being a force source. We choose the coefficients  $C_0$  and  $C_2$  such that the boundary conditions on the spherical surface are satisfied. We assume a finite slip at the spherical surface and split the boundary conditions at the surface into a kinematic and the Navier boundary condition [81]. At  $|r| = a$ , the normal component of the fluid velocity equals the normal component of the sphere velocity, i.e.,  $\tilde{v}_j^{\text{SP}}(\omega) = \delta_{ij} \tilde{V}_i^{\text{SP}}(\omega)$ . The kinematic boundary condition can be written as

$$6\pi \tilde{\eta}(\omega) a \hat{r}_i G_{ij}^{\text{SP}}(\omega) = \hat{r}_j, \quad (\text{A20})$$

from which the sphere velocity follows as  $\tilde{V}_i^{\text{SP}}(\omega) = \tilde{F}_i(\omega) / 6\pi \tilde{\eta}(\omega) a$ . Note that only in the zero-frequency limit does the source force  $\tilde{F}_i(\omega)$  equal the actual force on the sphere. The Navier boundary condition for the tangential velocity at  $|r| = a$  is given by

$$b[\nabla_k \tilde{v}_i^{\text{SP}}(\omega) + \nabla_i \tilde{v}_k^{\text{SP}}(\omega)] \hat{r}_k \mathcal{L}_{li} = [\tilde{v}_i^{\text{SP}}(\omega) - \tilde{V}_i^{\text{SP}}(\omega)] \mathcal{L}_{li}, \quad (\text{A21})$$

where  $b$  is the slip length and we define the projection operator as  $\mathcal{L}_{li} = (\delta_{li} - \hat{r}_l \hat{r}_i)$ . The Navier boundary condition in terms

of the sphere Green's function reads

$$\begin{aligned} b[\nabla_k G_{ij}^{\text{sp}}(\omega) + \nabla_i G_{kj}^{\text{sp}}(\omega)]\hat{r}_k \mathcal{L}_{li} \\ = [G_{ij}^{\text{sp}}(\omega) - \delta_{ij}/6\pi\tilde{\eta}(\omega)a]\mathcal{L}_{li}. \end{aligned} \quad (\text{A22})$$

The final result for  $G_{ij}^{\text{sp}}(\vec{r}, \omega)$  reads, using Eq. (A15),

$$\begin{aligned} G_{ij}^{\text{sp}}(\vec{r}, \omega) &= \frac{1}{4\pi\tilde{\eta}(\omega)\alpha^2 r^3} \\ &\times \{\delta_{ij}(E_1[1 + r\alpha + r^2\alpha^2]e^{-r\alpha} - E_2[1 + r\lambda]e^{-r\lambda}) \\ &- 3\hat{r}_i\hat{r}_j(E_1[1 + r\alpha + r^2\alpha^2/3]e^{-r\alpha} \\ &- E_2[1 + r\lambda + r^2\lambda^2/3]e^{-r\lambda})\}, \end{aligned} \quad (\text{A23})$$

with the coefficients

$$E_1 = \frac{2}{3}e^{\hat{\alpha}} \frac{(1 + 2\hat{b})(3 + 3\hat{\lambda} + \hat{\lambda}^2)}{W}, \quad (\text{A24})$$

$$E_2 = \frac{2}{3}e^{\hat{\lambda}} \frac{(1 + 2\hat{b})(3 + 3\hat{\alpha} + \hat{\alpha}^2) + \hat{b}\hat{\alpha}^2(1 + \hat{\alpha})}{W}, \quad (\text{A25})$$

and

$$W = (2 + 2\hat{\lambda} + \hat{\lambda}^2)(1 + \hat{b}(3 + \hat{\alpha})) + (1 + \hat{\alpha})(1 + 2\hat{b})\hat{\lambda}^2/\hat{\alpha}^2. \quad (\text{A26})$$

We define the dimensionless slip length,  $\hat{b} = b/a$ , and the dimensionless decay constants  $\hat{\alpha} = \alpha a$  and  $\hat{\lambda} = \lambda a$ . The corresponding friction function  $\tilde{\Gamma}^{\text{hyd}}(\omega)$  is given by

$$\delta_{ij}\tilde{\Gamma}^{\text{hyd}}(\omega) = \frac{\tilde{F}_i^{\text{sp}}(\omega)}{\tilde{V}_j^{\text{sp}}(\omega)} = -6\pi\tilde{\eta}(\omega)a \int d^3r \hat{r}_k \sigma_{kij} \delta(|r| - a). \quad (\text{A27})$$

For the hydrodynamic force  $\tilde{F}_i^{\text{sp}}(\omega)$  on a spherical particle, we use the projection of the stress tensor on the surface and integrate it over the sphere surface. Using Eq. (A17), and the derivative of  $G_{ij}^{\text{sp}}(\vec{r}, \omega)$  in Eq. (A23), we obtain the friction function of the spherical particle

$$\begin{aligned} \tilde{\Gamma}^{\text{hyd}}(\omega) &= \frac{4\pi\tilde{\eta}(\omega)a}{3} W^{-1} \{(1 + \hat{\lambda})(9 + 9\hat{\alpha} + \hat{\alpha}^2)(1 + 2\hat{b}) \\ &+ (1 + \hat{\alpha})[2\hat{\lambda}^2(1 + 2\hat{b}) + \hat{b}\hat{\alpha}^2(1 + \hat{\lambda})]\}, \end{aligned} \quad (\text{A28})$$

where we use the identities  $\int d^3r \delta_{ij} \delta(|r| - a) = 4\pi a^2 \delta_{ij}$  and  $\int d^3r \hat{r}_i \hat{r}_j \delta(|r| - a) = 4\pi a^2 \delta_{ij}/3$ . Assuming negligible slip, i.e.,  $b \rightarrow 0$ , and vanishing compressibility, i.e.,  $\lambda \rightarrow 0$ , we have

$$\tilde{\Gamma}^{\text{hyd}}(\omega) = 6\pi a \tilde{\eta}(\omega) (1 + \alpha a + a^2 \alpha^2 / 9). \quad (\text{A29})$$

Thus, the frequency-dependent hydrodynamic force on a spherical particle, i.e.,  $\tilde{F}_i^{\text{sp}}(\omega) = -\tilde{\Gamma}^{\text{hyd}}(\omega) \tilde{V}_i^{\text{sp}}(\omega)$ , is in the same limit given by

$$\tilde{F}_i^{\text{sp}}(\omega) = -6\pi a \tilde{\eta}(\omega) \tilde{V}_i^{\text{sp}}(\omega) (1 + \alpha a + a^2 \alpha^2 / 9). \quad (\text{A30})$$

## APPENDIX B: FLUID MOMENTUM AROUND A MOVING SPHERE

From the velocity field around the sphere, i.e.,  $\tilde{v}_i^{\text{sp}}(\vec{r}, \omega) = \tilde{F}_j(\vec{r}, \omega) G_{ij}^{\text{sp}}(\vec{r}, \omega)$ , and the expression in Eq. (A23), we can calculate the fluid momentum outside the moving sphere as

$$\tilde{p}_i(\omega) = \rho_0 \int_{|r|>a} \tilde{v}_i^{\text{sp}}(\vec{r}, \omega) d^3r. \quad (\text{B1})$$

We assume that the force source is oscillating along the  $x$  direction, i.e.,  $\vec{\tilde{F}}(\omega) = (\tilde{F}(\omega), 0, 0)^T$ , so that the momentum points in the  $x$  direction. The volume integral in Eq. (B1) involves the angular integrals

$$\begin{aligned} \int_{|r|>a} d^3r \delta_{ij} &= \int_a^\infty r^2 dr \int_0^\pi d\theta \sin\theta \int_0^{2\pi} d\Phi \delta_{ij}, \\ &= 4\pi \delta_{ij} \int_a^\infty r^2 dr, \end{aligned} \quad (\text{B2})$$

$$\begin{aligned} \int_{|r|>a} d^3r \hat{r}_i \hat{r}_j &= \int_a^\infty r^2 dr \int_0^\pi d\theta \sin\theta \cos^2\theta \int_0^{2\pi} d\Phi \delta_{ij} \\ &= 2\pi \delta_{ij} \int_a^\infty r^2 dr \int_{-1}^1 du u^2 \\ &= \frac{4}{3}\pi \delta_{ij} \int_a^\infty r^2 dr. \end{aligned} \quad (\text{B3})$$

In the derivation of the flow field around a sphere in Appendix A, we use the kinematic boundary condition Eq. (A20) and obtain the sphere velocity  $\tilde{V}_i^{\text{sp}}(\omega) = \tilde{F}_i(\omega)/6\pi\tilde{\eta}(\omega)a$ , such that in the low-frequency (steady) limit and without slip, the source force equals the actual force on the sphere. Using the identities in Eq. (B2) and (B3) and the expression in Eq. (A23) and inserting them into Eq. (B1), we arrive at

$$\begin{aligned} \tilde{p}_i(\omega) &= 6\pi \frac{\rho_0}{\alpha^2} a \tilde{V}_i^{\text{sp}}(\omega) \int_a^\infty \frac{1}{r} dr \\ &\times \{\delta_{ij}(E_1[1 + r\alpha + r^2\alpha^2]e^{-r\alpha} - E_2[1 + r\lambda]e^{-r\lambda}) \\ &- \delta_{ij}(E_1[1 + r\alpha + r^2\alpha^2/3]e^{-r\alpha} \\ &- E_2[1 + r\lambda + r^2\lambda^2/3]e^{-r\lambda})\} \end{aligned} \quad (\text{B4})$$

$$= 6\pi \frac{\rho_0}{\alpha^2} a \tilde{V}_i^{\text{sp}}(\omega) \int_a^\infty dr \left[ \frac{2}{3} E_1 r \alpha^2 e^{-r\alpha} + \frac{1}{3} E_2 r \lambda^2 e^{-r\lambda} \right] \quad (\text{B5})$$

$$= -6\pi \frac{\rho_0}{\alpha^2} a \tilde{V}_i^{\text{sp}}(\omega) \left[ \frac{2}{3} E_1 [e^{-r\alpha} (r\alpha + 1)]_a^\infty + \frac{1}{3} E_2 [e^{-r\lambda} (r\lambda + 1)]_a^\infty \right] \quad (\text{B6})$$

$$= 6\pi \frac{\rho_0}{\alpha^2} a \tilde{V}_i^{\text{sp}}(\omega) \left[ \frac{2}{3} E_1 [e^{-\alpha a} (\alpha a + 1)] + \frac{1}{3} E_2 [e^{-\lambda a} (\lambda a + 1)] \right], \quad (\text{B7})$$

For  $b \rightarrow 0$  and  $\lambda \rightarrow 0$ , the constants  $E_1$  and  $E_2$  in Eqs. (A24) and (A25) become  $E_1 = e^{\alpha a}$  and  $E_2 = (1 + \alpha a + a^2 \alpha^2 / 3)$ , and we obtain for the momentum

$$\tilde{p}_i(\omega) = 6\pi \frac{\rho_0}{\alpha^2} a \tilde{V}_i^{\text{sp}}(\omega) (1 + \alpha a + a^2 \alpha^2 / 9). \quad (\text{B8})$$

Using that the force is given by  $\tilde{F}_i = i\omega \tilde{p}_i$ , we obtain

$$\tilde{F}_i(\omega) = 6\pi a \tilde{\eta}(\omega) \tilde{V}_i^{\text{sp}}(\omega) (1 + \alpha a + a^2 \alpha^2 / 9), \quad (\text{B9})$$

which is (except the sign) identical to the result obtained in Eq. (A30) from integrating the surface force over the oscillating sphere. Thus, the net frequency-dependent momentum of the fluid inside the sphere vanishes, and there is no added-mass contribution due to the motion of the liquid inside the

sphere. It follows that the friction  $\tilde{\Gamma}^{\text{hyd}}$  calculated from hydrodynamic theory equals the friction  $\Gamma(t)$  extracted from single-particle trajectories using the GLE, and no correction for the fluid mass inside the sphere has to be applied.

### APPENDIX C: SIMULATION SETUP

We perform all MD simulations using the GROMACS simulation package [82] (version 2020-Modified). For water, we use the SPC/E [83] and TIP4P/2005 [84] rigid water models. We pre-equilibrate the system in an NPT ensemble ( $P = 1$  bar) using a Berendsen barostat [85] set to 1 atm. For production runs, we perform all simulations in the NVT ensemble with a temperature of  $T = 300$  K, controlled with a velocity rescaling thermostat [86]. For electrostatics, we use the particle-mesh Ewald method [87], with a cutoff length of 1 nm. We allow simulations to run for 600 ns, using integration time steps of 1 fs. We perform simulations in a  $(3.56 \text{ nm})^3$  cubic box with 1250 water molecules. From this simulation, we use the stress tensor trajectory of the whole system with a time step of  $\Delta t = 1$  fs to compute the shear and volume viscosity spectra as described in Appendix D.

For the results we show in Fig. 4, we run an MD simulation of SPC/E water with a total length of  $1 \mu\text{s}$  and a time step of 2 fs, and use the trajectories of 15 traced water particles for the memory kernel extraction. For the results we show in Appendix H, we additionally run simulations with integration time steps of 1 and 4 fs, and use the trajectories of two traced water particles for the memory kernel extraction.

For the Lennard-Jones (LJ) fluid, we simulate a system at  $T = 92$  K with a box length of 5 nm and 2744 LJ particles. For the particles, we took the Lennard-Jones parameters of argon of the GROMOS53a6 force field [88] ( $\sigma = 3.410 \text{ \AA}$ ,  $\epsilon = 0.996 \text{ kJ/mol}$  and a cutoff radius of  $2.5\sigma$ ). Using LJ units, the systems are at  $T^* = 0.77$  and  $P^* = 0.04$  corresponding to the liquid phase [89,90]. The system is first equilibrated in the NPT ensemble ( $P = 17$  bar) followed by a production run in the NVT ensemble for 10 ns with a time step of 2 fs. We use the stress tensor of the whole system to compute the shear and volume viscosities and the trajectories of 50 LJ particles for the memory kernel extraction.

### APPENDIX D: CALCULATION OF FREQUENCY-DEPENDENT SHEAR AND VOLUME VISCOSITY SPECTRA FROM MD SIMULATIONS

The shear viscosity kernel  $\eta(t)$  is given by the trace-free part of the stress tensor by the Green-Kubo relation [2,36,41,80]

$$\begin{aligned} \tilde{\eta}(\vec{k} = 0, \omega) &= \int_0^\infty dt \eta(t) e^{-i\omega t} \\ &= \frac{V}{6k_B T} \int_0^\infty e^{-i\omega t} \sum_{i \neq j} \langle \Pi_{ij}(t) \Pi_{ij}(0) \rangle dt, \end{aligned} \quad (\text{D1})$$

where  $V$  is the volume of the fluid. We define the trace-free part of the stress tensor  $\sigma_{ij}$  as

$$\Pi_{ij} = \sigma_{ij} - \delta_{ij} \frac{1}{3} \sum_k \sigma_{kk}, \quad (\text{D2})$$

where  $i, j \in \{x, y, z\}$ .

We use the fluctuations of the instantaneous pressure from its average value  $\langle P \rangle$ , i.e.,  $\delta P(t) = P(t) - \langle P \rangle$ , to compute the volume viscosity kernel  $\zeta(t)$ .  $P(t)$  is computed from the trace of the stress tensor, i.e.,  $P(t) = \frac{1}{3} \sum_k \sigma_{kk}(t)$ . Using the half-sided Fourier transformation, we compute the volume viscosity spectrum via [34]

$$\begin{aligned} \tilde{\zeta}(\vec{k} = 0, \omega) &= \int_0^\infty dt \zeta(t) e^{-i\omega t} \\ &= \frac{V}{k_B T} \int_0^\infty e^{-i\omega t} \langle \delta P(t) \delta P(0) \rangle dt. \end{aligned} \quad (\text{D3})$$

For the Fourier transformation of the viscosity data, and the memory kernel data as well, we use the fast Fourier transform (FFT) algorithm implemented in NumPy version 1.18.5 [91], where we assume the input signal  $x(t)$  to be single-sided, i.e.,  $x(t < 0) = 0$ . All data in the time domain are truncated at 10 ps.

### APPENDIX E: FITTING OF THE VISCOSITY DATA

We fit the real part of the Fourier-transformed viscosity spectra  $\tilde{\eta}(\omega)$  and  $\tilde{\zeta}(\omega)$  extracted from the MD simulation by a combination of six and five exponential-oscillating components according to Eqs. (10) and (12), respectively, using the Levenberg-Marquardt algorithm implemented in scipy ver. 1.4 [92]. The initial values for all  $\eta_{0,j}$ ,  $\tau_{n,j}$ , and  $\tau_{o,j}$  are chosen suitably; the same for  $\zeta_{0,j}$ ,  $\tau_{v,j}$ , and  $\tau_{w,j}$ . We constrain the parameter space to positive values. We filter the data set beforehand on a logarithmic frequency scale to reduce the overall number of data points to fit. We also weight the data exponentially so that the data for small frequencies become more important for the fit. After optimizing the parameters, we use them as initial parameters to perform the final fit of the data in the time domain. Here the input data are filtered on the logarithmic time-domain scale but without exponential weighting. This allows us to fit the low- and high-frequency regimes at the same time. The obtained fit parameters are summarized in Appendix F.

### APPENDIX F: SUMMARY OF FITTING PARAMETERS

This appendix summarizes the fitting parameters in Tables I–III.

### APPENDIX G: COMPONENTS OF THE SHEAR VISCOSITY FOR SPC/E WATER

The fitting components according to Eq. (9) and the fitting parameters in Table I (Appendix F) for the SPC/E water MD simulation are depicted in Fig. 8, together with the MD data and the total fit shown in Fig. 1.

For  $\tau_{o,j} \lesssim 2\tau_{n,j}$  the relaxation mode is underdamped and characterized by an oscillation period  $\approx \tau_{o,j}$ , for  $\tau_{o,j} \gtrsim 2\tau_{n,j}$  the mode is overdamped and characterized by the decay time  $\tau_{o,j}^2/\tau_{n,j}$ .

TABLE I. Fitting parameters for the viscoelastic model of the shear viscosity in Eqs. (9) and (10) to MD data of the SPC/E water model and the TIP4P/2005 water model. The timescales are converted to frequencies for ease of comparison with Figs. 1(a)–1(c).

Parameter	SPC/E	TIP4P/2005
$\eta_{0,I}$	0.45 mPa s	0.25 mPa s
$(2\pi\tau_{n,I})^{-1}$	1.96 THz	1.83 THz
$(2\pi\tau_{o,I})^{-1}$	0.67 THz	0.47 THz
$\eta_{0,II}$	0.14 mPa s	0.06 mPa s
$(2\pi\tau_{n,II})^{-1}$	3.33 THz	1.94 THz
$(2\pi\tau_{o,II})^{-1}$	1.69 THz	1.54 THz
$\eta_{0,III}$	0.08 mPa s	0.06 mPa s
$(2\pi\tau_{n,III})^{-1}$	5.45 THz	4.16 THz
$(2\pi\tau_{o,III})^{-1}$	8.08 THz	7.74 THz
$\eta_{0,IV}$	0.02 mPa s	0.43 mPa s
$(2\pi\tau_{n,IV})^{-1}$	10.58 THz	2.04 THz
$(2\pi\tau_{o,IV})^{-1}$	15.50 THz	0.76 THz
$\eta_{0,V}$	0.005 mPa s	0.02 mPa s
$(2\pi\tau_{n,V})^{-1}$	27.47 THz	20.95 THz
$(2\pi\tau_{o,V})^{-1}$	31.74 THz	17.03 THz
$\eta_{0,VI}$	$3.31 \times 10^{-5}$ mPa s	$8.11 \times 10^{-4}$ mPa s
$(2\pi\tau_{n,VI})^{-1}$	6.31 THz	15.61 THz
$(2\pi\tau_{o,VI})^{-1}$	42.10 THz	39.73 THz

#### APPENDIX H: FRICTION FROM MD SIMULATIONS WITH DIFFERENT TIME RESOLUTION

In Fig. 9, we investigate the influence of the MD simulation time resolution on the extracted friction function, where we simulated SPC/E water with different time steps. The memory kernel, extracted as explained in Appendix L, exhibits, besides numerical noise, no distinct differences between the different time resolutions. All important features we observe in the memory kernel for 1 fs are also visible for the longer time

TABLE II. Fitting parameters for the viscoelastic model of the volume viscosity in Eqs. (11) and (12) to MD data of the SPC/E water model and the TIP4P/2005 water model. The time scales are converted to frequencies for ease of comparison with Figs. 1(d)–1(f).

Parameter	SPC/E	TIP4P/2005
$\zeta_{0,I}$	0.75 mPa s	0.23 mPa s
$(2\pi\tau_{v,I})^{-1}$	1.11 THz	0.13 THz
$(2\pi\tau_{w,I})^{-1}$	0.41 THz	0.09 THz
$\zeta_{0,II}$	0.45 mPa s	1.23 mPa s
$(2\pi\tau_{v,II})^{-1}$	1.53 THz	1.14 THz
$(2\pi\tau_{w,II})^{-1}$	0.75 THz	0.50 THz
$\zeta_{0,III}$	0.44 mPa s	0.55 mPa s
$(2\pi\tau_{v,III})^{-1}$	5.52 THz	7.96 THz
$(2\pi\tau_{w,III})^{-1}$	3.55 THz	4.14 THz
$\zeta_{0,IV}$	0.04 mPa s	0.01 mPa s
$(2\pi\tau_{v,IV})^{-1}$	6.89 THz	4.33 THz
$(2\pi\tau_{w,IV})^{-1}$	7.07 THz	7.10 THz
$\zeta_{0,V}$	0.02 mPa s	0.02 mPa s
$(2\pi\tau_{v,V})^{-1}$	20.76 THz	19.39 THz
$(2\pi\tau_{w,V})^{-1}$	18.20 THz	17.88 THz

TABLE III. Fitting parameters for the viscoelastic model of the shear viscosity in Eqs. (9), (10) and volume viscosity in Eqs. (11), (12) to MD data of the LJ fluid. The time scales are converted to frequencies for ease of comparison with Figs. 12(a) and 12(b).

Parameter	$\eta$	$\zeta$
$\eta_{0,I}, \zeta_{0,I}$	0.12 mPa s	0.23 mPa s
$(2\pi\tau_{n,I})^{-1}, (2\pi\tau_{v,I})^{-1}$	2.38 THz	70.71 THz
$(2\pi\tau_{o,I})^{-1}, (2\pi\tau_{w,I})^{-1}$	1.18 THz	40.69 THz
$\eta_{0,II}, \zeta_{0,II}$	0.05 mPa s	0.05 mPa s
$(2\pi\tau_{n,II})^{-1}, (2\pi\tau_{v,II})^{-1}$	4.04 THz	6.12 THz
$(2\pi\tau_{o,II})^{-1}, (2\pi\tau_{w,II})^{-1}$	2.41 THz	3.06 THz
$\eta_{0,III}, \zeta_{0,III}$	0.07 mPa s	0.32 mPa s
$(2\pi\tau_{n,III})^{-1}, (2\pi\tau_{v,III})^{-1}$	32.87 THz	15.32 THz
$(2\pi\tau_{o,III})^{-1}, (2\pi\tau_{w,III})^{-1}$	19.25 THz	11.09 THz
$\eta_{0,IV}, \zeta_{0,IV}$	0.01 mPa s	0.01 mPa s
$(2\pi\tau_{n,IV})^{-1}, (2\pi\tau_{v,IV})^{-1}$	449.15 THz	987.59 THz
$(2\pi\tau_{o,IV})^{-1}, (2\pi\tau_{w,IV})^{-1}$	333.42 THz	18.07 THz

steps in Fig. 9. The same is expected for the extracted viscosity spectra in Fig. 1, since they stem from the same molecular features. Deviations in the viscosity spectrum in Fig. 1(b) start around 30–60 THz, below the frequency where discretization effects are expected to be important for  $\Delta t = 1$  fs, which rules out discretization effects as the cause for the deviations between MD data and viscosity model seen in Fig. 1(b). At higher frequencies, in the resolution limit regime, the real part data in Fig. 9(b) is dominated by noise, which means that we cannot make a statement about the actual scaling at these frequencies. For the 1 fs data (black), the data points become noisy around 100 THz, which is a fifth of the maximal frequency of 500 THz. This suggests that our used FFT algorithm explained in Appendix E is numerically unstable in this frequency regime, and data points in this regime should not be interpreted.

#### APPENDIX I: FRICTION OF A SPHERE FOR FREQUENCY-INDEPENDENT VISCOSITIES

In Fig. 10, we show the calculated hydrodynamic friction of a sphere according to Eq. (2) for constant shear viscosity  $\tilde{\eta}(\omega) = \eta_0$  for different sphere radii  $a$ . Note that we here use a vanishing volume viscosity  $\tilde{\zeta} = 0$ , for better comparability with the results in Ref. [37]. As already discussed in Ref. [37], the friction sensitively depends on the slip length  $b$  and its real and imaginary parts both increase as  $\omega \rightarrow \infty$ . Note that the high-frequency behavior of the imaginary part differs from the results in Ref. [37], as we use a different definition of the Fourier transformation. We refer to Ref. [37] for a detailed discussion and point out that the addition of frequency-dependent shear and volume viscosity significantly changes the friction, as shown in Fig. 2.

#### APPENDIX J: LOW- AND HIGH-FREQUENCY SCALING OF THE HYDRODYNAMIC FRICTION OF A SPHERE

In the following, we analyze the friction in Eq. (2). For the real part of the friction in Eq. (2), we analytically obtain the asymptotic behavior (for finite  $c$  and  $b \neq 0$ ) for shear viscosity

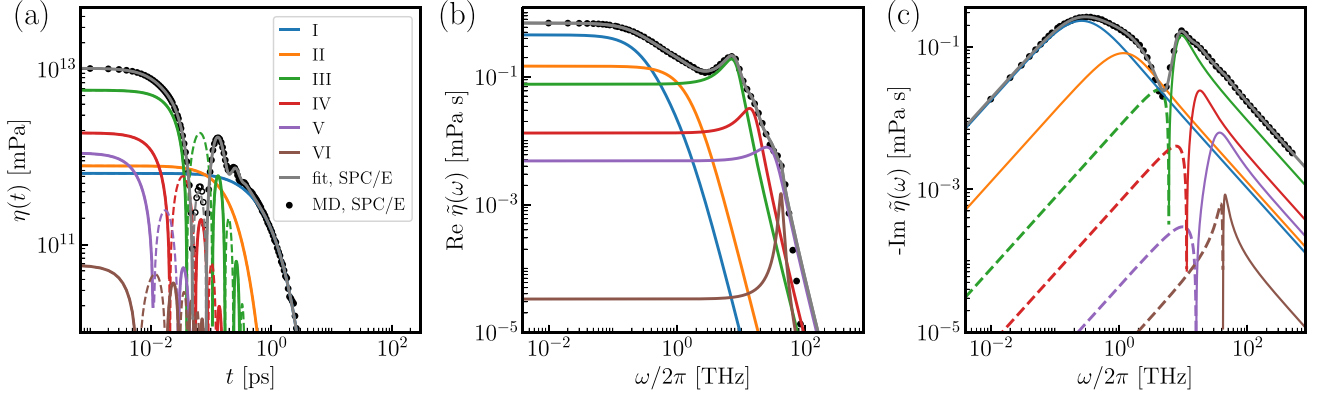


FIG. 8. Extracted shear viscosity  $\eta$  from MD simulations of SPC/E water (shown in Fig. 1) together with the fitting components (lines) according to Eq. (9) using the fitting parameters in Table I (Appendix F). Dashed lines and empty circles denote negative values.

and volume viscosity given by the models in Eqs. (10) and (12) as

$$\frac{\text{Re } \tilde{\Gamma}^{\text{hyd}}(\omega)}{6\pi\eta_0 a} \simeq \begin{cases} \omega \rightarrow 0 & \frac{1+2b}{1+3b} + \frac{a(1+2b)^2\sqrt{\rho_0/\eta_0}}{\sqrt{2(1+3b)^2}}\omega^{1/2} \\ & + O(\omega^{3/2}) \\ \omega \rightarrow \infty & \\ \text{if } \tilde{\zeta} = \zeta_0 & \frac{2a}{9}\Phi\frac{(\alpha_\infty)^2}{2\lambda_c}\omega^{1/2} \\ \text{otherwise} & \frac{2a}{9}\Phi\frac{(\alpha_\infty)^2}{\lambda_\infty}\omega^0, \end{cases} \quad (\text{J1})$$

with the constants

$$\Phi = \left( \sum_{j=1}^{VI} \frac{\eta_{0,j}\tau_{n,j}}{\tau_{o,j}^2} \right) / \eta_0, \quad (\text{J2})$$

$$\eta_0 = \sum_{j=1}^{VI} \eta_{0,j}. \quad (\text{J3})$$

Here, we introduced high-frequency limiting values for the inverse length scales  $\alpha_\infty$ ,  $\lambda_\infty$ , and  $\lambda_c$  given as

$$\alpha(\omega \rightarrow \infty) \equiv \alpha_\infty = \sqrt{\rho_0\tilde{\eta}_\infty}, \quad (\text{J4})$$

$$\lambda_\infty = \sqrt{\rho_0\tilde{Z}_\infty},$$

$$\lambda_c = \sqrt{\rho_0/2 \sum_{j=1}^V \zeta_{0,j}}, \quad (\text{J5})$$

where  $\tilde{\eta}_\infty$  and  $\tilde{Z}_\infty$  follow from the high-frequency limits of the shear and volume viscosities in Eqs. (10) and (12), with

$$\bullet \Delta t = 1 \text{ fs} \quad \bullet \Delta t = 2 \text{ fs} \quad \bullet \Delta t = 4 \text{ fs}$$

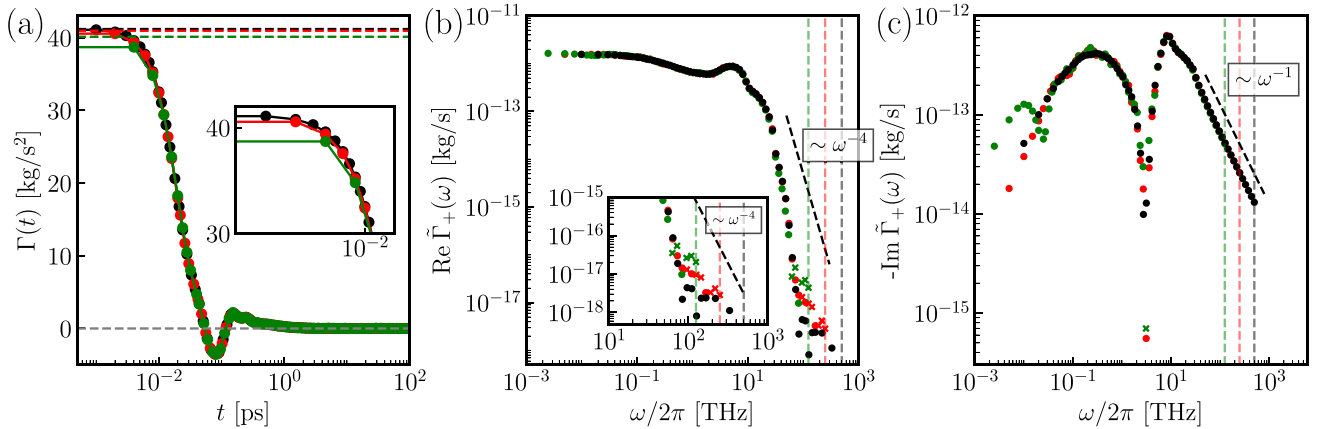


FIG. 9. Influence of the MD simulation time resolution on the frequency-dependent friction. We show (a) the extracted water memory kernel  $\Gamma(t)$  (extracted as explained in Appendix L) and (b), (c) the real and imaginary part of the Fourier-transformed  $\tilde{\Gamma}_+(\omega)$  for SPC/E water MD simulations with different time resolutions as explained in Appendix C. In the frequency domain, circles denote positive values, and crosses denote negative values. The colored horizontal dashed lines in the time domain (a) denote the initial values of the memory kernel data  $\Gamma(0)$ . The colored vertical dashed lines in the frequency domain in panels (b) and (c) denote the maximal frequencies of the Fourier-transformed data.

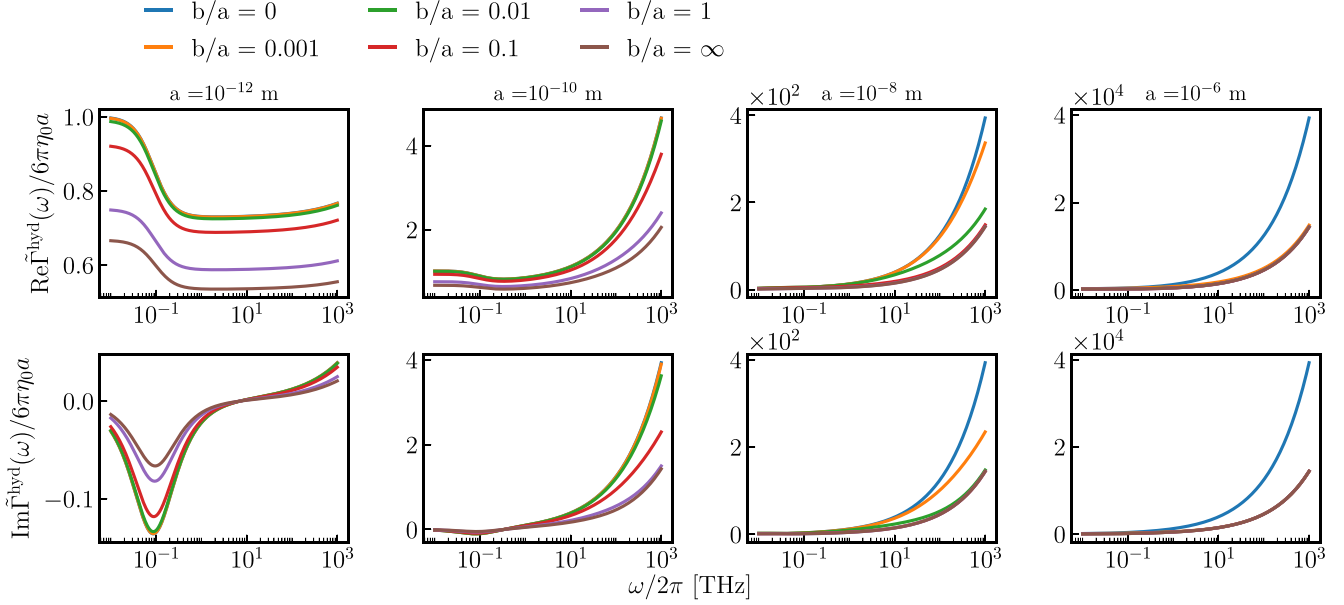


FIG. 10. Real and imaginary parts of the rescaled friction function of a sphere  $\tilde{\Gamma}^{\text{hyd}}(\omega) = \text{Re } \tilde{\Gamma}^{\text{hyd}}(\omega) + i \text{Im } \tilde{\Gamma}^{\text{hyd}}(\omega)$  given by Eq. (2), for various slip parameters  $\hat{b}$  and sphere radii  $a$ . Here we use a constant shear viscosity of  $\eta_0 = 1$  mPa s, the water density  $\rho_0 = 10^3$  kg/m<sup>3</sup>,  $c = 10^3$  m/s, and vanishing volume viscosity  $\tilde{\zeta} = 0$  for comparability with the results in Ref. [37].

$\tilde{Z}(\omega) = 4\tilde{\eta}(\omega)/3 + \tilde{\zeta}(\omega) - i\rho_0 c^2/\omega$ , as

$$\tilde{\eta}_\infty = \left( \sum_{j=l}^{VI} \frac{\eta_{0,j} \tau_{n,j}}{\tau_{o,j}^2} \right)^{-1}, \quad (\text{J6})$$

$$\tilde{Z}_\infty = \left( \sum_{j=l}^{VI} \frac{4\eta_{0,j} \tau_{n,j}}{3\tau_{o,j}^2} + \sum_{j=l}^V \frac{\zeta_{0,j} \tau_{v,j}}{\tau_{w,j}^2} + \rho_0 c^2 \right)^{-1}. \quad (\text{J7})$$

For  $\tilde{\zeta}(\omega) \neq \tilde{\zeta}_0$ , the real part of the friction  $\tilde{\Gamma}^{\text{hyd}}(\omega)$  in Eq. (J1) converges for  $\omega \rightarrow \infty$  to a constant value depending on the steady-state viscosity constants and relaxation times. This stems from our choice of exponential-oscillatory models for shear and volume viscosity, for which the real part of the components scales as  $\omega^{-4}$  and the imaginary part scales as  $\omega^{-1}$ . The friction in the frequency domain differs only marginally for frequency-dependent volume viscosity and for vanishing volume viscosity, i.e., for  $\tilde{\zeta} = 0$ . For  $\tilde{\zeta} = 0$ , the friction has the same asymptotic behavior as for  $\tilde{\zeta}(\omega)$  in Eq. (J1), with modified constants. In contrast, for  $\tilde{\zeta} = \zeta_0$ , the real part diverges, as visible in Fig. 3.

In the absence of slip, i.e., for  $b = 0$ , the real part scales as

$$\frac{\text{Re } \tilde{\Gamma}^{\text{hyd}}(\omega)}{6\pi \eta_0 a} \simeq \begin{cases} \omega \rightarrow 0 & 1 + \frac{a\sqrt{\rho_0/\eta_0}}{\sqrt{2}} \omega^{1/2} + O(\omega^{3/2}) \\ \omega \rightarrow \infty & \\ \text{if } \tilde{\zeta} = \zeta_0 & \frac{2a}{9} \Phi \frac{(\alpha_\infty)^2}{2\lambda_c} \omega^{1/2} \\ \text{otherwise} & \frac{2a}{9} \Phi \frac{\alpha_\infty(\alpha_\infty + 2\lambda_\infty)}{\lambda_\infty} \omega^0. \end{cases} \quad (\text{J8})$$

By comparison with Eq. (J1), we see that the plateau value for  $\omega \rightarrow \infty$  and frequency-dependent  $\tilde{\zeta}$  depends on whether the slip length is zero or not, but the high-frequency scaling for  $\tilde{\zeta} = \zeta_0$  is slip-independent.

For completeness, the imaginary part of the friction function for  $b \neq 0$  has the asymptotic scaling

$$\frac{\text{Im } \tilde{\Gamma}^{\text{hyd}}(\omega)}{6\pi \eta_0 a} \simeq \begin{cases} \omega \rightarrow 0 & \frac{a(1+2\hat{b})^2 \sqrt{\omega \rho_0 / \eta_0}}{\sqrt{2}(1+3\hat{b})^2} + O(\omega) \\ \omega \rightarrow \infty & \\ \text{if } \tilde{\zeta} = \zeta_0 & \frac{2}{9a} \Phi \frac{(\alpha_\infty)^2}{2\lambda_c} \omega^{1/2} \\ \text{otherwise} & -\frac{2a}{9} \Phi C_\infty \omega^{-1}, \end{cases} \quad (\text{J9})$$

where the constant  $C_\infty$  is given by

$$C_\infty = 4 + \frac{2}{\hat{b}} - \frac{(\alpha_\infty)^2}{(\lambda_\infty)^2}. \quad (\text{J10})$$

We see that for vanishing volume viscosity, i.e.,  $\tilde{\zeta}(\omega) \rightarrow 0$  as  $\omega \rightarrow \infty$ , the imaginary part of the friction decays as  $\sim \omega^{-1}$  for high frequencies, but diverges with the same scaling  $\sim \omega^{1/2}$  as the real part for  $\tilde{\zeta} = \zeta_0$ .

For the stick case ( $b \rightarrow 0$ ) the imaginary part scales as

$$\frac{\text{Im } \tilde{\Gamma}^{\text{hyd}}(\omega)}{6\pi \eta_0 a} \simeq \begin{cases} \omega \rightarrow 0 & -\frac{a\sqrt{\omega \rho_0 / \eta_0}}{\sqrt{2}} + O(\omega) \\ \omega \rightarrow \infty & \\ \text{if } \tilde{\zeta} = \zeta_0 & \frac{2}{9} \Phi \frac{(\alpha_\infty)^2 a}{2\lambda_c} \omega^{1/2} \\ \text{otherwise} & -\frac{2a}{9} \Phi \frac{\alpha_\infty(\alpha_\infty - 4\lambda_\infty)}{(\lambda_\infty)^2} \omega^{-1}. \end{cases} \quad (\text{J11})$$

## APPENDIX K: DERIVATION OF THE HYDRODYNAMIC TAIL

Applying the inverse Fourier transformation in Eq. (A30) leads to the Boussinesq-Basset equation [4,20,39]. We

decompose the total force in Eq. (A30) into three parts:

$$\tilde{F}_{i,1}^{\text{SP}}(\omega) = -6\pi a\tilde{\eta}(\omega)\tilde{V}_i^{\text{SP}}(\omega), \quad (\text{K1})$$

$$\tilde{F}_{i,2}^{\text{SP}}(\omega) = -6\pi a^2\sqrt{\tilde{\eta}(\omega)\rho_0 i\omega}\tilde{V}_i^{\text{SP}}(\omega), \quad (\text{K2})$$

$$\tilde{F}_{i,3}^{\text{SP}}(\omega) = -\frac{2}{3}\pi a^3\rho_0 i\omega\tilde{V}_i^{\text{SP}}(\omega). \quad (\text{K3})$$

Assuming a frequency-independent shear viscosity, i.e.,  $\tilde{\eta}(\omega) = \eta_0$ , it is easily seen that in the time-domain, the first component is given by  $F_{i,1}^{\text{SP}}(t) = -6\pi a\eta_0 V_i^{\text{SP}}(t)$  and the third component by  $F_{i,3}^{\text{SP}}(t) = -\frac{2}{3}\pi\rho_0 a^3 \dot{V}_i^{\text{SP}}(t)$ . To derive the expression for the second component, we use  $\tilde{V}_i^{\text{SP}}(\omega) = \dot{V}_i^{\text{SP}}(\omega)/i\omega$ , where the dot denotes the time derivative. For the expression  $\tilde{F}_{i,2}^{\text{SP}}(\omega) = -6\pi a^2\sqrt{\frac{\eta_0\rho_0}{i\omega}}\dot{V}_i^{\text{SP}}(\omega) = -6\pi a^2\sqrt{\eta_0\rho_0}\tilde{g}(\omega)\dot{V}_i^{\text{SP}}(\omega)$ ,  $\tilde{g}(\omega)$  in the time domain is given by  $g(t) = \frac{\Theta(t)}{\sqrt{\pi}}t^{-1/2}$ :

$$\tilde{g}(\omega) = \frac{1}{\sqrt{\pi}}\int_0^\infty e^{-i\omega t} \frac{dt}{t^{1/2}} \quad (\text{K4})$$

$$= \frac{1}{\sqrt{\pi i\omega}}\int_0^\infty e^{-s} \frac{ds}{s^{1/2}} \quad (\text{K5})$$

$$= \frac{1}{\sqrt{\pi i\omega}}\int_0^\infty e^{-s} \frac{ds}{s^{1/2}} \quad (\text{K6})$$

$$= \frac{1}{\sqrt{i\omega}}, \quad (\text{K7})$$

where we use a Wick rotation to arrive at Eq. (K6) from Eq. (K5). Applying the convolution theorem in the inverse Fourier transformation of the second force component in Eq. (K2), the full force is given by the Boussinesq-Basset equation

$$F_i^{\text{SP}}(t) = -6\pi a\eta V_i^{\text{SP}}(t) - 6a^2\sqrt{\pi\eta_0\rho_0}\int_0^t dt' \frac{\dot{V}_i^{\text{SP}}(t')}{\sqrt{t-t'}} - \frac{2}{3}\pi\rho_0 a^3 \dot{V}_i^{\text{SP}}(t). \quad (\text{K8})$$

The first term in Eq. (K8) is the steady Stokes drag. The third term is known as the added mass term, proportional to the mass  $m_0 = \frac{2}{3}\pi\rho_0 a^3$ . It reflects that an unsteadily moving sphere must accelerate the surrounding fluid volume. The second term, including a convolution integral, describes the sphere's history of motion, also known as the Basset history force. Applying a partial integration on this term, we obtain

$$F_{i,2}^{\text{SP}}(t) = 3a^2\sqrt{\pi\eta_0\rho_0}\int_0^t dt' (t-t')^{-3/2}V_i^{\text{SP}}(t') + V_i^{\text{SP}}(t)f(0) - V_i^{\text{SP}}(0)f(t), \quad (\text{K9})$$

where  $f(t) = \theta(t)6a^2\sqrt{\pi\eta_0\rho_0}t^{-1/2}$ . We see that the memory kernel predicted by continuum hydrodynamics consists of the power-law decay

$$\lim_{t \rightarrow \infty} \Gamma^{\text{hyd}}(t) \approx -3a^2\sqrt{\pi\eta_0\rho_0}t^{-3/2}, \quad (\text{K10})$$

which is the famous hydrodynamic tail [4,71,72]. The Volterra equation in Eq. (L5) relates the long-time behavior of the memory kernel and the velocity autocorrelation function

$C^{vv}(t)$  (VACF). Using the expression in Eq. (16), we find that, for long times, the VACF scales as

$$\lim_{t \rightarrow \infty} C^{vv}(t) \approx \frac{k_B T \sqrt{\rho_0}}{12} (\pi\eta_0 t)^{-3/2}. \quad (\text{K11})$$

## APPENDIX L: CALCULATION OF THE FREQUENCY-DEPENDENT FRICTION FROM SIMULATION TRAJECTORIES

Various data-based methods to estimate the parameters of the GLE from experimental or simulation trajectories have been proposed [6,8,11,93–96]. A robust and computationally efficient technique to extract the memory kernel from given time series trajectories can be derived by multiplying Eq. (6) for the position  $x(t)$  with the initial velocity  $\dot{x}(0)$ . Taking the ensemble average leads to an equation involving correlation functions that is calculated from the given trajectory [11,97,98]. By this, we obtain a Volterra equation of the first kind [9,44]:

$$mC^{\dot{x}\dot{x}}(t) = -\int_0^t dt' \Gamma(t')C^{\dot{x}\dot{x}}(t-t'), \quad (\text{L1})$$

where  $C^{\dot{x}\dot{x}}(t) = \langle \dot{x}(0)\dot{x}(t) \rangle$  and  $C^{\dot{x}\dot{x}}(t) = \langle \dot{x}(0)\dot{x}(t) \rangle$ , and we use that  $\nabla U = 0$  and that  $\dot{x}(0)$  and  $F_R(t)$  are uncorrelated, i.e.,  $\langle \dot{x}(0)F_R(t) \rangle = 0$  [1].

Analyses for one-dimensional trajectories have shown that compared to the direct method [11], extraction of the memory kernel's running integral produces significantly more stable results [9]. We integrate Eq. (L1) over time

$$m[C^{\dot{x}\dot{x}}(t) - C^{\dot{x}\dot{x}}(0)] = -\int_0^t ds \int_0^s ds' \Gamma(s')C^{\dot{x}\dot{x}}(s-s') \quad (\text{L2})$$

$$= -\int_0^t ds' \int_{s'}^t ds \Gamma(s-s')C^{\dot{x}\dot{x}}(s') \quad (\text{L3})$$

$$= -\int_0^t ds' \int_0^{t-s'} du \Gamma(u)C^{\dot{x}\dot{x}}(s') \quad (\text{L4})$$

$$= -\int_0^t ds G(t-s)C^{\dot{x}\dot{x}}(s), \quad (\text{L5})$$

where  $G(t) = \int_0^t ds \Gamma(s)$  is the running integral of the memory kernel. Discretizing this equation with a time step  $\Delta t$ , we obtain an iterative formula for  $G_i = G(i\Delta t)$ . For a discretized correlation function we use the short-hand notation  $C_i^{AB} = \langle A(0)B(i\Delta t) \rangle$ . For the running integral of the memory kernel  $G_i$ , we obtain from Eq. (L5) by applying the trapezoidal rule on the integral:

$$G_i = \left[ m(C_0^{\dot{x}\dot{x}} - C_i^{\dot{x}\dot{x}}) - \Delta t \sum_{j=1}^{i-1} G_j C_{i-j}^{\dot{x}\dot{x}} \right] \left( \frac{1}{2} \Delta t C_0^{\dot{x}\dot{x}} \right)^{-1}, \quad (\text{L6})$$

where we use  $G_0 = 0$ . If we compute the velocity autocorrelation function  $C_i^{\dot{x}\dot{x}}$  from the given time series  $x(t)$ , we can use Eq. (L6) to determine the running integral  $G(t)$  and based on this the memory kernel  $\Gamma(t)$  by differentiation.

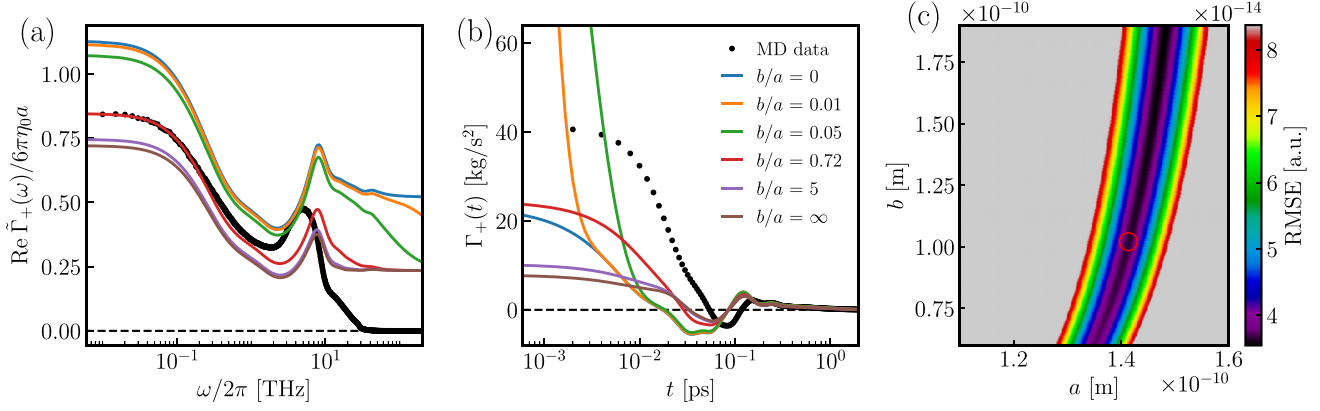


FIG. 11. Influence of the slip length  $b$  on the hydrodynamic friction. (a) Real part of the friction function  $\text{Re } \tilde{\Gamma}_+(\omega)$  in Fig. 4 for different slip lengths  $\hat{b} = b/a$  with fixed radius  $a = 0.14$  nm. (b) Friction  $\Gamma_+(t)$  in the time domain obtained by numerical inverse Fourier transformation. (c) Root mean squared error (RMSE) between the MD data of the real part of the friction  $\text{Re } \tilde{\Gamma}_+(\omega)$  in Fig. 4 (black), and the prediction from Eq. (2) in dependence of the sphere radius  $a$  and the slip length  $b$ . The red circle denotes the optimal parameter combination corresponding to the result shown as a green line in Fig. 4 and shown as red lines in panels (a) and (b).

#### APPENDIX M: FREQUENCY-DEPENDENT FINITE-SIZE CORRECTION FOR MEMORY KERNELS

Numerical predictions of the velocity autocorrelation function and the frequency-dependent friction of a particle in a fluid are significantly affected by the presence of periodic boundary conditions and finite system sizes in molecular dynamics simulations [42]. We follow the procedure elaborated in Ref. [44] which yields an analytic correction term for the frequency-dependent friction that accounts for periodic boundary effects. From the uncorrected friction  $\tilde{\Gamma}_+(\omega)$ , the corrected version is computed by

$$[\tilde{\Gamma}_+^{\text{corr}}(\omega)]^{-1} = [\tilde{\Gamma}_+(\omega)]^{-1} - \Delta G^{\text{corr}}(\omega), \quad (\text{M1})$$

where the frequency-dependent correction term  $\Delta G^{\text{corr}}(\omega)$  is given by

$$\Delta G^{\text{corr}}(\omega) = \left[ \sum_{\vec{n}, \vec{n} \neq 0} \frac{1}{3} \text{Tr}[G_{ij}(\vec{n}L, \omega)] \right] - \frac{1}{3L^3} \int d\vec{r}' \text{Tr}[G_{ij}(\vec{r}', \omega)]. \quad (\text{M2})$$

$L$  is the box size, here  $L = 3.5616$  nm for the water simulation and  $L = 4.5$  nm for the methane in water simulation [9],  $\vec{n} = n_x \vec{e}_x + n_y \vec{e}_y + n_z \vec{e}_z$  is a lattice vector with  $n_x, n_y, n_z$  integers, and  $\vec{e}_i$  are the unit vectors in the directions  $x, y$ , and  $z$ .  $\text{Tr}$  denotes the tensor trace.  $G$  is the Green's function given in Eq. (A15), derived in Appendix A. For a detailed description of the numerical calculation of the correction term in Eq. (M2), we refer to Ref. [44]. We additionally correct the velocity autocorrelation function  $\tilde{C}_+^{vv}(\omega)$  from the MD simulations by the correction term

$$\tilde{C}_+^{vv, \text{corr}}(\omega) = \frac{\tilde{C}_+^{vv}(\omega)}{1 + (k_B T)^{-1} \tilde{C}_+^{vv}(\omega) \tilde{\Gamma}_+^{\text{corr}}(\omega) \tilde{\Gamma}_+(\omega) \Delta G^{\text{corr}}(\omega)}, \quad (\text{M3})$$

which is derived using Eq. (16). The corrected data  $\tilde{\Gamma}_+^{\text{corr}}(\omega)$  and  $\tilde{C}_+^{vv, \text{corr}}(\omega)$  is shown in Figs. 4–6 as black circles. Note

that for the calculation of the PBC correction, we used the fitted frequency-dependent viscosity models shown in Fig. 1 as it improves the finite-size correction [44].

#### APPENDIX N: DETERMINATION OF THE EFFECTIVE RADIUS AND THE SLIP LENGTH

In Fig. 11, we investigate the dependence of the hydrodynamic friction  $\text{Re } \tilde{\Gamma}_+(\omega)$  on the hydrodynamic radius  $a$  and the slip length  $b$ . We observe a significant dependence on the slip length in Fig. 11(a), where higher slip leads to lower friction. The same is visible in the time domain in Fig. 11(b), obtained from Fig. 11(a) by applying the inverse Fourier transformation on  $\tilde{\Gamma}_+(\omega)$ .

The slip length influences for not too high frequencies only the magnitude of the friction function. In Fig. 11(c), we show the root mean squared error (RMSE) between the MD data of the real part of the friction  $\text{Re } \tilde{\Gamma}_+(\omega)$  [Fig. 4(b), black], and the prediction from Eq. (2) in dependence of the sphere radius  $a$  and the slip length  $b$ . We find a global minimum, denoted as a red circle, which corresponds to the results reported in Fig. 4 and shown as a red line in Figs. 11(a) and 11(b). Due to the anisotropic dependence of the error in Fig. 11(c) on  $a$  and  $b$ , we can fit the effective radius  $a$  much more accurately than the slip length  $b$ . Hence, the estimation of the slip length by this procedure is subject to considerable uncertainty.

#### APPENDIX O: RESULTS FOR A LENNARD-JONES FLUID

We compare simulation results and hydrodynamic theory for a Lennard-Jones (LJ) particle in a LJ fluid (see Appendix C for simulation details). In Figs. 12(a) and 12(b) we show the extracted and fitted viscoelastic spectra of the MD simulation. Note that, in contrast to the water system, we use four viscoelastic fitting components for both shear and volume viscosity and we do not subtract finite-size effects here, as we are only interested in the behavior in the low- and intermediate-frequency regime. The extracted friction  $\tilde{\Gamma}_+(\omega)$  in Figs. 12(c) and 12(d) (circles) agrees for low

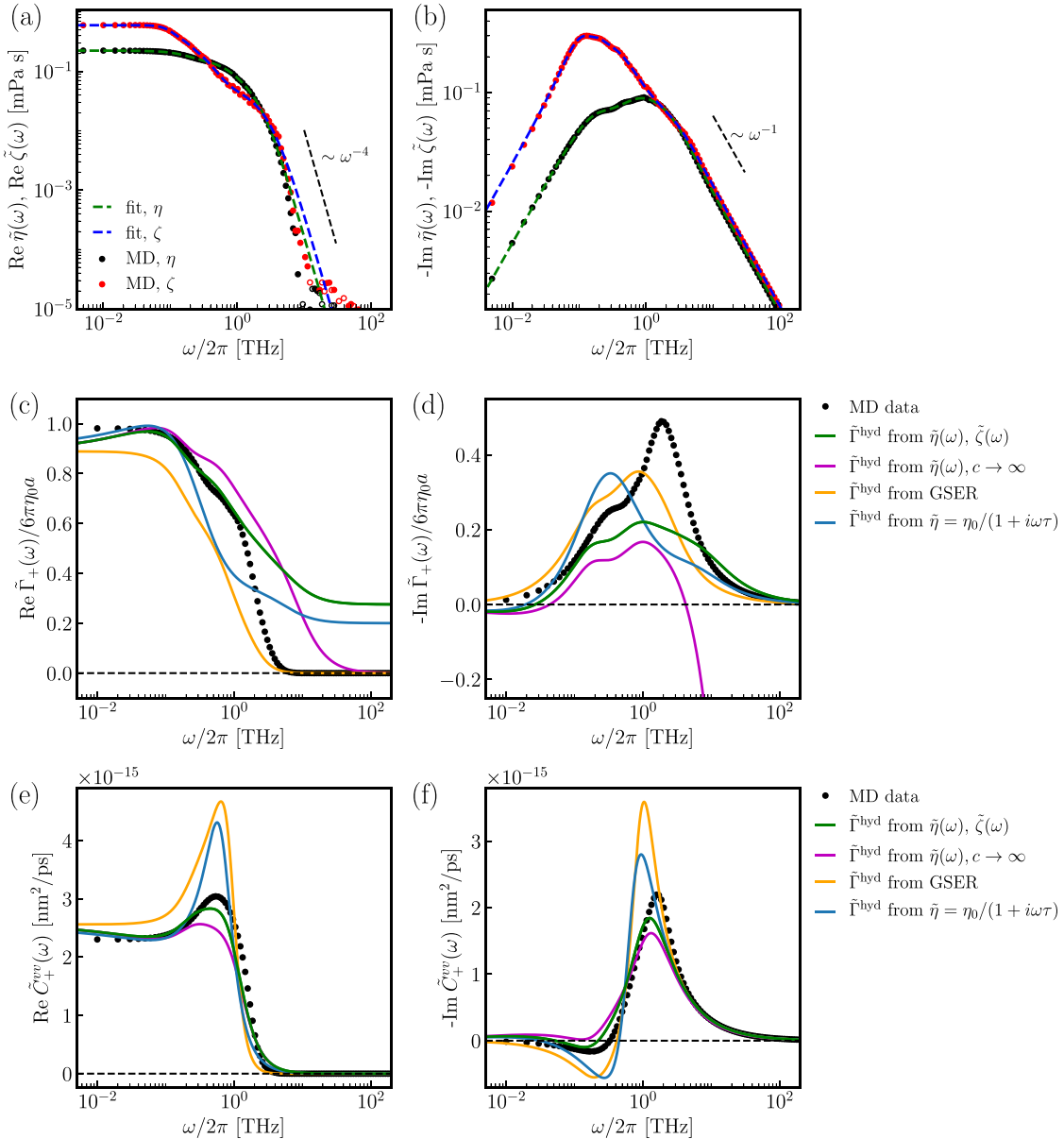


FIG. 12. Simulation results and hydrodynamic theory for a Lennard-Jones particle in a Lennard-Jones fluid. (a), (b) Extracted shear viscosity  $\eta$  and volume viscosity  $\zeta$  in frequency space from MD simulations (circles) with fits (dashed lines) according to Eq. (10) and the fitting parameters in Table III (Appendix F). Empty circles denote negative values. Note that all data are shown in logarithmic spacing for better visibility. (c), (d) Real and imaginary part of the Fourier transformed friction  $\tilde{\Gamma}_+(\omega)$  extracted from MD simulations using the GLE (circles). We compare with the results from Eq. (2) (green) for  $a = 0.13$  nm and  $\hat{b} = b/a = 0.17$  and the shear and volume viscosity parameters given in Appendix F. We also compare with the hydrodynamic prediction neglecting compressibility, i.e.,  $c \rightarrow \infty$  (purple), and additionally neglecting shear-wave effects, i.e.,  $\alpha \rightarrow 0$  [yellow, Eq. (13)]. The blue lines show the hydrodynamic friction using a Maxwell model fit of the shear viscosity to the MD friction data and vanishing volume viscosity. The fitting constants are  $\eta_0 = 0.23$  mPa s and  $(2\pi\tau)^{-1} = 0.34$  THz. (e), (f) Comparison between the frequency-dependent velocity autocorrelation function  $\tilde{C}_+^{vv}(\omega)$  of a LJ particle in a LJ fluid from the MD and the hydrodynamic prediction in Eq. (16), which we obtain using the results shown in panels (c) and (d).

frequencies well with the hydrodynamic prediction using the fitted viscosity models (green lines), the agreement is worse with the model neglecting compressibility, i.e.,  $c \rightarrow \infty$  (purple lines), and the GSER (yellow lines). We use  $\rho_0 = 1370$  kg/m<sup>3</sup> and  $c = 869$  m/s [44]. Even if no distinct peaks can be seen in the friction spectrum, several viscoelastic components are still necessary for the modeling, as a simple Maxwell model (blue) deviates significantly from the MD

data in Figs. 12(c) and 12(d). As for the water results in Fig. 4, a plateau can be seen in the real part of the hydrodynamic friction prediction for frequencies above 10 THz, which is not present in the MD data. We conclude that the hydrodynamic prediction with the frequency-dependent viscosity functions and finite compressibility is most appropriate, which becomes even more evident when analyzing the VACF in Figs. 12(e) and 12(f).

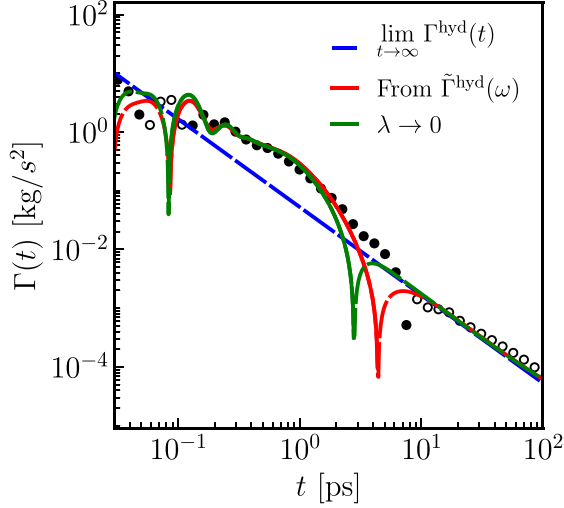


FIG. 13. Discussion of the influence of compressibility on the hydrodynamic long-time tail. We compare the long-time behavior of the water memory kernel from MD simulations (circles) with the numerical inverse Fourier transformation of the hydrodynamic friction  $\tilde{\Gamma}^{\text{hyd}}(\omega)$  in Eq. (2) for the compressible case (red line) and in the incompressible limit  $\lambda \rightarrow 0$  (green line). Dashed lines and empty circles denote negative values.

#### APPENDIX P: LONG-TIME BEHAVIOR OF THE WATER MEMORY KERNEL WITH COMPRESSIBILITY

In Fig. 13, we compare the long-time behavior of the water memory kernel from MD simulations (circles) with the numerical inverse Fourier transformation of the hydrodynamic friction  $\Gamma^{\text{hyd}}(\omega)$  in Eq. (2) for the compressible case (red line) and in the incompressible limit  $\lambda \rightarrow 0$  (green line). As discussed in the main text, the hydrodynamic tail remains unchanged in the incompressible case. The sign change from positive to negative values around 3 ps is slightly shifted to earlier times.

#### APPENDIX Q: DERIVATION OF EQ. (16)

We start from the Fourier-transformed GLE in Eq. (8), i.e.,  $\tilde{v}(\omega) = i\omega\tilde{\chi}(\omega)\tilde{F}_R(\omega)$ , where  $\tilde{v}(\omega) = i\omega\tilde{x}(\omega)$  and  $\tilde{\chi}(\omega) = [i\omega\tilde{\Gamma}_+(\omega) - m\omega^2]^{-1}$ . The relation  $\langle F_R(t)F_R(t') \rangle = k_B T \Gamma(|t-t'|)$  in Fourier space reads

$$\langle \tilde{F}_R(\omega)\tilde{F}_R(\omega') \rangle = k_B T \int_{-\infty}^{\infty} dt e^{-i\omega t} \int_{-\infty}^{\infty} dt' e^{-i\omega' t'} \Gamma(t-t') \quad (\text{Q1})$$

$$= k_B T \int_{-\infty}^{\infty} dt' e^{-i(\omega+\omega')t} \times \int_{-\infty}^{\infty} dt e^{-i\omega(t-t')} \Gamma(t-t') \quad (\text{Q2})$$

$$= k_B T \int_{-\infty}^{\infty} dt' e^{-i(\omega+\omega')t'} \tilde{\Gamma}(\omega) \quad (\text{Q3})$$

$$= 2\pi k_B T \delta(\omega + \omega') \tilde{\Gamma}(\omega). \quad (\text{Q4})$$

Using this identity, we obtain the Fourier transformation of the VACF:

$$\tilde{C}^{vv}(\omega) = \int_{-\infty}^{\infty} \frac{d\omega'}{2\pi} e^{-i\omega(t-t')} \langle \tilde{v}(\omega)\tilde{v}(\omega') \rangle \quad (\text{Q5})$$

$$= \int_{-\infty}^{\infty} \frac{d\omega'}{2\pi} \langle i\omega\tilde{x}(\omega)i\omega'\tilde{x}(\omega') \rangle \quad (\text{Q6})$$

$$= - \int_{-\infty}^{\infty} \frac{d\omega'}{2\pi} \langle \omega\tilde{\chi}(\omega)\tilde{F}_R(\omega)\omega'\tilde{\chi}(\omega')\tilde{F}_R(\omega') \rangle \quad (\text{Q7})$$

$$= -k_B T \int_{-\infty}^{\infty} d\omega'\omega\omega'\tilde{\chi}(\omega)\tilde{\chi}(\omega')\delta(\omega + \omega')\tilde{\Gamma}(\omega) \quad (\text{Q8})$$

$$= k_B T \omega^2 \tilde{\chi}(\omega)\tilde{\chi}(-\omega)\tilde{\Gamma}(\omega) \quad (\text{Q9})$$

$$= k_B T \omega^2 \tilde{\Gamma}(\omega) \frac{\tilde{\chi}(-\omega) - \tilde{\chi}(\omega)}{\frac{1}{\tilde{\chi}(\omega)} - \frac{1}{\tilde{\chi}(-\omega)}} \quad (\text{Q10})$$

$$= k_B T \omega^2 \tilde{\Gamma}(\omega) \frac{\tilde{\chi}(-\omega) - \tilde{\chi}(\omega)}{i\omega[\tilde{\Gamma}_+(\omega) + \tilde{\Gamma}_+(-\omega)]}. \quad (\text{Q11})$$

Since  $\chi(t)$  is a real function, we have  $\tilde{\chi}(-\omega) - \tilde{\chi}(\omega) = \tilde{\chi}^*(\omega) - \tilde{\chi}(\omega) = -2i \text{Im} \tilde{\chi}(\omega)$ , where  $\tilde{\chi}^*(\omega)$  is the complex conjugate of  $\tilde{\chi}(\omega)$ . For any function  $f(t)$  symmetric in  $t$ , such as  $\Gamma(t)$  and  $C^{vv}(t)$ , we have

$$\tilde{f}_+(\omega) + \tilde{f}_+(-\omega) = \tilde{f}_+(\omega) + \tilde{f}_+^*(\omega) \quad (\text{Q12})$$

$$= \int_{-\infty}^{\infty} dt f_+(t) e^{-i\omega t} + \int_{-\infty}^{\infty} dt f_+(t) e^{i\omega t} \quad (\text{Q13})$$

$$= \int_{-\infty}^{\infty} dt f(t) \theta(t) e^{-i\omega t} + \int_{-\infty}^{\infty} dt f(t) \theta(-t) e^{-i\omega t} \quad (\text{Q14})$$

$$= \tilde{f}(\omega). \quad (\text{Q15})$$

Inserting this identity for  $\tilde{\Gamma}_+(\omega)$  into Eq. (Q11), we obtain the fluctuation-dissipation theorem:

$$\tilde{C}^{vv}(\omega) = -2k_B T \omega \text{Im} \tilde{\chi}(\omega), \quad (\text{Q16})$$

and

$$\text{Re} \tilde{C}_+^{vv}(\omega) = -k_B T \omega \text{Im} \tilde{\chi}(\omega), \quad (\text{Q17})$$

$$= k_B T \omega \text{Re}[i\tilde{\chi}(\omega)], \quad (\text{Q18})$$

where we used  $\tilde{C}^{vv}(\omega) = \tilde{C}_+^{vv}(\omega) + [\tilde{C}_+^{vv}(\omega)]^* = 2\text{Re}\tilde{C}_+^{vv}(\omega)$ . For the single-sided VACF, we finally obtain

$$\tilde{C}_+^{vv}(\omega) = i\omega k_B T \tilde{\chi}(\omega) = \frac{i\omega k_B T}{i\omega\tilde{\Gamma}_+(\omega) - m\omega^2}, \quad (\text{Q19})$$

which is Eq. (16) in the main text. Here, by employing the Kramers-Kronig relations, we use the fact that if the real parts of the Fourier transformations of two half-sided time-domain functions are equal [Eq. (Q18)], the total complex functions are equal [9].

- [1] H. Mori, Transport, collective motion, and Brownian motion, *Prog. Theor. Phys.* **33**, 423 (1965).
- [2] R. Zwanzig, Time-correlation functions and transport coefficients in statistical mechanics, *Annu. Rev. Phys. Chem.* **16**, 67 (1965).
- [3] A. Carof, R. Vuilleumier, and B. Rotenberg, Two algorithms to compute projected correlation functions in molecular dynamics simulations, *J. Chem. Phys.* **140**, 124103 (2014).
- [4] D. Lesnicki, R. Vuilleumier, A. Carof, and B. Rotenberg, Molecular hydrodynamics from memory kernels, *Phys. Rev. Lett.* **116**, 147804 (2016).
- [5] C. Ayaz, L. Salfi, B. A. Dalton, and R. R. Netz, Generalized Langevin equation with a nonlinear potential of mean force and nonlinear memory friction from a hybrid projection scheme, *Phys. Rev. E* **105**, 054138 (2022).
- [6] G. Jung, M. Hanke, and F. Schmid, Iterative reconstruction of memory kernels, *J. Chem. Theory Comput.* **13**, 2481 (2017).
- [7] G. Jung and F. Schmid, Frequency-dependent hydrodynamic interaction between two solid spheres, *Phys. Fluids* **29**, 126101 (2017).
- [8] J. O. Daldrop, B. G. Kowalik, and R. R. Netz, External potential modifies friction of molecular solutes in water, *Phys. Rev. X* **7**, 041065 (2017).
- [9] B. Kowalik, J. O. Daldrop, J. Kappler, J. C. F. Schulz, A. Schlaich, and R. R. Netz, Memory-kernel extraction for different molecular solutes in solvents of varying viscosity in confinement, *Phys. Rev. E* **100**, 012126 (2019).
- [10] B. G. Mitterwallner, C. Schreiber, J. O. Daldrop, J. O. Rädler, and R. R. Netz, Non-Markovian data-driven modeling of single-cell motility, *Phys. Rev. E* **101**, 032408 (2020).
- [11] J. O. Daldrop, J. Kappler, F. N. Brüning, and R. R. Netz, Butane dihedral angle dynamics in water is dominated by internal friction, *Proc. Natl. Acad. Sci. USA* **115**, 5169 (2018).
- [12] C. Ayaz, L. Tepper, F. N. Brüning, J. Kappler, J. O. Daldrop, and R. R. Netz, Non-Markovian modeling of protein folding, *Proc. Natl. Acad. Sci. USA* **118**, e2023856118 (2021).
- [13] B. A. Dalton, C. Ayaz, H. Kiefer, A. Klimek, L. Tepper, and R. R. Netz, Fast protein folding is governed by memory-dependent friction, *Proc. Natl. Acad. Sci. USA* **120**, e2220068120 (2023).
- [14] B. A. Dalton, H. Kiefer, and R. R. Netz, The role of memory-dependent friction and solvent viscosity in isomerization kinetics in viscogenic media, *Nat. Commun.* **15**, 3761 (2024).
- [15] B. A. Dalton and R. R. Netz, pH modulates friction memory effects in protein folding, *Phys. Rev. Lett.* **133**, 188401 (2024).
- [16] P. Sollich, F. Lequeux, P. Hébraud, and M. E. Cates, Rheology of soft glassy materials, *Phys. Rev. Lett.* **78**, 2020 (1997).
- [17] D. Mizuno, C. Tardin, C. F. Schmidt, and F. C. MacKintosh, Nonequilibrium mechanics of active cytoskeletal networks, *Science* **315**, 370 (2007).
- [18] D. Winter, J. Horbach, P. Virnau, and K. Binder, Active nonlinear microrheology in a glass-forming Yukawa fluid, *Phys. Rev. Lett.* **108**, 028303 (2012).
- [19] T. Hiraiwa and R. R. Netz, Systematic bottom-up theory for the viscoelastic response of worm-like chain networks, *Europhys. Lett.* **123**, 58002 (2018).
- [20] T. S. Chow and J. J. Hermans, Effect of inertia on the Brownian motion of rigid particles in a viscous fluid, *J. Chem. Phys.* **56**, 3150 (1972).
- [21] T. S. Chow and J. J. Hermans, Brownian motion of a spherical particle in a compressible fluid, *Physica* **65**, 156 (1973).
- [22] E. H. Hauge and A. Martin-Löf, Fluctuating hydrodynamics and Brownian motion, *J. Stat. Phys.* **7**, 259 (1973).
- [23] D. Bedeaux and P. Mazur, A generalization of Faxén's theorem to nonsteady motion of a sphere through a compressible fluid in arbitrary flow, *Physica* **78**, 505 (1974).
- [24] E. J. Hinch, Application of the Langevin equation to fluid suspensions, *J. Fluid Mech.* **72**, 499 (1975).
- [25] P. Español, On the propagation of hydrodynamic interactions, *Physica A* **214**, 185 (1995).
- [26] B. U. Felderhof, Backtracking of a sphere slowing down in a viscous compressible fluid, *J. Chem. Phys.* **123**, 044902 (2005).
- [27] D. Chakraborty, Velocity autocorrelation function of a Brownian particle, *Eur. Phys. J. B* **83**, 375 (2011).
- [28] R. Tatsumi and R. Yamamoto, Direct numerical simulation of dispersed particles in a compressible fluid, *Phys. Rev. E* **85**, 066704 (2012).
- [29] K. Mizuta, Y. Ishii, K. Kim, and N. Matubayasi, Bridging the gap between molecular dynamics and hydrodynamics in nanoscale Brownian motions, *Soft Matter* **15**, 4380 (2019).
- [30] R. Zwanzig and M. Bixon, Hydrodynamic theory of the velocity correlation function, *Phys. Rev. A* **2**, 2005 (1970).
- [31] H. Metiu, D. W. Oxtoby, and K. F. Freed, Hydrodynamic theory for vibrational relaxation in liquids, *Phys. Rev. A* **15**, 361 (1977).
- [32] W. M. Slie, A. R. Donfor, Jr., and T. A. Litovitz, Ultrasonic shear and longitudinal measurements in aqueous glycerol, *J. Chem. Phys.* **44**, 3712 (1966).
- [33] M. Pelton, D. Chakraborty, E. Malachosky, P. Guyot-Sionnest, and J. E. Sader, Viscoelastic flows in simple liquids generated by vibrating nanostructures, *Phys. Rev. Lett.* **111**, 244502 (2013).
- [34] J. S. Medina, R. Prosmi, P. Villarreal, G. Delgado-Barrio, G. Winter, B. González, J. V. Alemán, and C. Collado, Molecular dynamics simulations of rigid and flexible water models: Temperature dependence of viscosity, *Chem. Phys.* **388**, 9 (2011).
- [35] G. S. Fanourgakis, J. S. Medina, and R. Prosmi, Determining the bulk viscosity of rigid water models, *J. Phys. Chem. A* **116**, 2564 (2012).
- [36] J. C. F. Schulz, A. Schlaich, M. Heyden, R. R. Netz, and J. Kappler, Molecular interpretation of the non-Newtonian viscoelastic behavior of liquid water at high frequencies, *Phys. Rev. Fluids* **5**, 103301 (2020).
- [37] A. Erbaş, R. Podgornik, and R. R. Netz, Viscous compressible hydrodynamics at planes, spheres and cylinders with finite surface slip, *Eur. Phys. J. E* **32**, 147 (2010).
- [38] S. Zendeheroud, J. O. Daldrop, Y. von Hansen, H. Kiefer, and R. R. Netz, Molecular Stokes-Einstein and Stokes-Einstein-Debye relations for water including viscosity-dependent slip and hydrodynamic radius, *Phys. Rev. E* **110**, 064610 (2024).
- [39] J. Boussinesq, *Théorie Analytique de la Chaleur (in French)* (Gauthier-Villars, Paris, 1903), Vol. 2, p. 172.
- [40] B. J. Alder and T. E. Wainwright, Decay of the velocity autocorrelation function, *Phys. Rev. A* **1**, 18 (1970).
- [41] J.-P. Hansen and I. R. McDonald, *Theory of Simple Liquids With Applications to Soft Matter* (Academic Press, Amsterdam, Boston, 2013).
- [42] I.-C. Yeh and G. Hummer, System-size dependence of diffusion coefficients and viscosities from molecular dynamics

- simulations with periodic boundary conditions, *J. Phys. Chem. B* **108**, 15873 (2004).
- [43] A. J. Asta, M. Levesque, R. Vuilleumier, and B. Rotenberg, Transient hydrodynamic finite-size effects in simulations under periodic boundary conditions, *Phys. Rev. E* **95**, 061301(R) (2017).
- [44] L. Scalfi, D. Vitali, H. Kiefer, and R. R. Netz, Frequency-dependent hydrodynamic finite size correction in molecular simulations reveals the long-time hydrodynamic tail, *J. Chem. Phys.* **158**, 191101 (2023).
- [45] R. F. Schmidt, H. Kiefer, R. Dalgliesh, M. Gradzielski, and R. R. Netz, Nanoscopic interfacial hydrogel viscoelasticity revealed from comparison of macroscopic and microscopic rheology, *Nano Lett.* **24**, 4758 (2024).
- [46] G. G. Stokes, On the effect of the internal friction of fluids on the motion of pendulums, *Cambridge Philos. Trans.* **9**, 8 (1851).
- [47] G. K. Batchelor, *An Introduction to Fluid Dynamics* (Cambridge University Press, Cambridge, 2000).
- [48] S. Kim and S. J. Karrila, *Microhydrodynamics: Principles and Selected Applications* (Courier Corporation, North Chelmsford, MA, 2013).
- [49] L. D. Landau and E. M. Lifshits, *Fluid Mechanics* (Pergamon Press, Oxford, UK, 1959), Vol. 11.
- [50] G. G. Stokes, On the theories of the internal friction of fluids in motion, and of the equilibrium and motion of elastic solids, *Trans. Camb. Philos. Soc.* **8**, 287 (1845).
- [51] F. Jaeger, O. K. Matar, and E. A. Müller, Bulk viscosity of molecular fluids, *J. Chem. Phys.* **148**, 174504 (2018).
- [52] K. R. Harris and L. A. Woolf, Temperature and volume dependence of the viscosity of water and heavy water at low temperatures, *J. Chem. Eng. Data* **49**, 1064 (2004).
- [53] F. Sedlmeier, S. Shadkhoo, R. Bruinsma, and R. R. Netz, Charge/mass dynamic structure factors of water and applications to dielectric friction and electroacoustic conversion, *J. Chem. Phys.* **140**, 054512 (2014).
- [54] L. D. Landau and E. M. Lifshitz, *Theoretical Physics 6: Fluid Mechanics*, 2nd ed. (Pergamon Press, New York, 1987), Chap. 108.
- [55] D. J. Acheson, *Elementary Fluid Dynamics* (Clarendon Press, Oxford, 1990).
- [56] I. P. Omelyan, I. M. Mryglod, and M. V. Tokarchuk, Wavevector- and frequency-dependent shear viscosity of water the modified collective mode approach and molecular dynamics calculations, *Condens. Matter Phys.* **8**, 25 (2005).
- [57] N. M. Lacevic and J. E. Sader, Viscoelasticity of glycerol at ultra-high frequencies investigated via molecular dynamics simulations, *J. Chem. Phys.* **144**, 054502 (2016).
- [58] T. J. O'Sullivan, S. K. Kannam, D. Chakraborty, B. D. Todd, and J. E. Sader, Viscoelasticity of liquid water investigated using molecular dynamics simulations, *Phys. Rev. Fluids* **4**, 123302 (2019).
- [59] L. Bocquet and E. Charlaix, Nanofluidics, from bulk to interfaces, *Chem. Soc. Rev.* **39**, 1073 (2010).
- [60] P. V. Ruijgrok, P. Zijlstra, A. L. Tchegotareva, and M. Orrit, Damping of acoustic vibrations of single gold nanoparticles optically trapped in water, *Nano Lett.* **12**, 1063 (2012).
- [61] A. Cunsolo, G. Ruocco, F. Sette, C. Masciovecchio, A. Mermet, G. Monaco, M. Sampoli, and R. Verbeni, Experimental determination of the structural relaxation in liquid water, *Phys. Rev. Lett.* **82**, 775 (1999).
- [62] D. M. Carey and G. M. Korenowski, Measurement of the Raman spectrum of liquid water, *J. Chem. Phys.* **108**, 2669 (1998).
- [63] S. Carlson, F. N. Brüning, P. Loche, D. J. Bonthuis, and R. R. Netz, Exploring the absorption spectrum of simulated water from MHz to Infrared, *J. Phys. Chem. A* **124**, 5599 (2020).
- [64] R. Schulz, Y. von Hansen, J. O. Daldrop, J. Kappler, F. Noé, and R. R. Netz, Collective hydrogen-bond rearrangement dynamics in liquid water, *J. Chem. Phys.* **149**, 244504 (2018).
- [65] S. Tazi, A. Boğan, M. Salanne, V. Marry, P. Turq, and B. Rotenberg, Diffusion coefficient and shear viscosity of rigid water models, *J. Phys.: Condens. Matter* **24**, 284117 (2012).
- [66] M. A. González and J. L. F. Abascal, A flexible model for water based on TIP4P/2005, *J. Chem. Phys.* **135**, 224516 (2011).
- [67] A. V. Straube, B. G. Kowalik, R. R. Netz, and F. Höfling, Rapid onset of molecular friction in liquids bridging between the atomistic and hydrodynamic pictures, *Commun. Phys.* **3**, 126 (2020).
- [68] T. G. Mason and D. A. Weitz, Optical measurements of frequency-dependent linear viscoelastic moduli of complex fluids, *Phys. Rev. Lett.* **74**, 1250 (1995).
- [69] T. M. Squires and T. G. Mason, Fluid mechanics of microrheology, *Annu. Rev. Fluid Mech.* **42**, 413 (2010).
- [70] S. L. Seyler and C. E. Seyler, Molecular hydrodynamic theory of the velocity autocorrelation function, *J. Chem. Phys.* **159**, 054108 (2023).
- [71] M. H. Ernst, E. H. Hauge, and J. M. J. Van Leeuwen, Asymptotic time behavior of correlation functions, *Phys. Rev. Lett.* **25**, 1254 (1970).
- [72] N. Corngold, Behavior of autocorrelation functions, *Phys. Rev. A* **6**, 1570 (1972).
- [73] L. Bocquet and J.-L. Barrat, Hydrodynamic boundary conditions and correlation functions of confined fluids, *Phys. Rev. Lett.* **70**, 2726 (1993).
- [74] T. Omori, N. Inoue, L. Joly, S. Merabia, and Y. Yamaguchi, Full characterization of the hydrodynamic boundary condition at the atomic scale using an oscillating channel: Identification of the viscoelastic interfacial friction and the hydrodynamic boundary position, *Phys. Rev. Fluids* **4**, 114201 (2019).
- [75] H. Oga, T. Omori, C. Herrero, S. Merabia, L. Joly, and Y. Yamaguchi, Theoretical framework for the atomistic modeling of frequency-dependent liquid-solid friction, *Phys. Rev. Res.* **3**, L032019 (2021).
- [76] Y. Uematsu, R. R. Netz, and D. J. Bonthuis, Analytical interfacial layer model for the capacitance and electrokinetics of charged aqueous interfaces, *Langmuir* **34**, 9097 (2018).
- [77] M. Baus and J. Wallenborn, Long-time behavior of the nonlocal shear viscosity of a one-component plasma: A microscopic approach, *J. Stat. Phys.* **16**, 91 (1977).
- [78] R. K. Agarwal, K.-Y. Yun, and R. Balakrishnan, Beyond Navier-Stokes: Burnett equations for flows in the continuum-transition regime, *Phys. Fluids* **13**, 3061 (2001).
- [79] P. J. Daivis and D. J. Evans, Comparison of constant pressure and constant volume nonequilibrium simulations of sheared model decane, *J. Chem. Phys.* **100**, 541 (1994).
- [80] D. J. Evans and G. P. Morriss, *Statistical Mechanics of Nonequilibrium Liquids* (Cambridge University Press, Cambridge, England, 2008).
- [81] C. L. Navier, Sur les lois du mouvement des fluides, *Mem. Acad. Royal Sci. Inst.* **6**, 389 (1823).

- [82] S. Pronk, S. Páll, R. Schulz, P. Larsson, P. Bjelkmar, R. Apostolov, M. R. Shirts, J. C. Smith, P. M. Kasson, D. van der Spoel *et al.*, GROMACS 4.5: A high-throughput and highly parallel open source molecular simulation toolkit, *Bioinformatics* **29**, 845 (2013).
- [83] H. J. C. Berendsen, T. P. Grigera, and J. R. Straatsma, The missing term in effective pair potentials, *J. Phys. Chem.* **91**, 6269 (1987).
- [84] J. L. F. Abascal and C. Vega, A general purpose model for the condensed phases of water: TIP4P/2005, *J. Chem. Phys.* **123**, 234505 (2005).
- [85] H. J. C. Berendsen, J. P. M. Postma, W. F. van Gunsteren, A. DiNola, and J. R. Haak, Molecular dynamics with coupling to an external bath, *J. Chem. Phys.* **81**, 3684 (1984).
- [86] G. Bussi, D. Donadio, and M. Parrinello, Canonical sampling through velocity rescaling, *J. Chem. Phys.* **126**, 014101 (2007).
- [87] T. Darden, D. York, and L. Pedersen, Particle mesh Ewald: An  $N\log(N)$  method for Ewald sums in large systems, *J. Chem. Phys.* **98**, 10089 (1993).
- [88] C. Oostenbrink, A. Villa, A. E. Mark, and W. F. Van Gunsteren, A biomolecular force field based on the free enthalpy of hydration and solvation: The GROMOS force-field parameter sets 53A5 and 53A6, *J. Comput. Chem.* **25**, 1656 (2004).
- [89] J. Vrabec, G. K. Kedia, G. Fuchs, and H. Hasse, Comprehensive study of the vapour-liquid coexistence of the truncated and shifted Lennard-Jones fluid including planar and spherical interface properties, *Mol. Phys.* **104**, 1509 (2006).
- [90] A. Ahmed and R. J. Sadus, Effect of potential truncations and shifts on the solid-liquid phase coexistence of Lennard-Jones fluids, *J. Chem. Phys.* **133**, 124515 (2010).
- [91] C. R. Harris, K. J. Millman, S. J. van der Walt, R. Gommers, P. Virtanen, D. Cournapeau, E. Wieser, J. Taylor, S. Berg, N. J. Smith, R. Kern, M. Picus, S. Hoyer, M. H. van Kerkwijk, M. Brett, A. Haldane, J. Fernández del Río, M. Wiebe, P. Peterson, P. Gérard-Marchant, K. Sheppard, T. Reddy *et al.*, Array programming with NumPy, *Nature (London)* **585**, 357 (2020).
- [92] P. Virtanen, R. Gommers, T. E. Oliphant, M. Haberland, T. Reddy, D. Cournapeau, E. Burovski, P. Peterson, W. Weckesser, J. Bright *et al.*, SciPy 1.0: Fundamental algorithms for scientific computing in python, *Nat. Meth.* **17**, 261 (2020).
- [93] O. F. Lange and H. Grubmüller, Collective Langevin dynamics of conformational motions in proteins, *J. Chem. Phys.* **124**, 214903 (2006).
- [94] V. Klippenstein and N. F. A. van der Vegt, Cross-correlation corrected friction in (generalized) Langevin models, *J. Chem. Phys.* **154**, 191102 (2021).
- [95] H. Vroylandt, L. Goudenège, P. Monmarché, F. Pietrucci, and B. Rotenberg, Likelihood-based non-Markovian models from molecular dynamics, *Proc. Natl. Acad. Sci. USA* **119**, e2117586119 (2022).
- [96] L. Tepper, B. A. Dalton, and R. R. Netz, Accurate memory kernel extraction from discretized time-series data, *J. Chem. Theor. Comput.* **20**, 3061 (2024).
- [97] B. J. Berne and G. D. Harp, On the calculation of time correlation functions, *Adv. Chem. Phys.* **17**, 63 (1970).
- [98] J. E. Straub, M. Borkovec, and B. J. Berne, Calculation of dynamic friction on intramolecular degrees of freedom, *J. Phys. Chem.* **91**, 4995 (1987).